

Decoupling of static and dynamic criticality in a driven Mott insulator

A. de la Torre,^{1,2} K. L. Seyler,^{1,2} M. Buchhold,^{1,2} Y. Baum,^{1,2} G. Zhang,³ N.J. Laurita,¹ J.W. Harter,^{1,2} L. Zhao,^{1,2} I. Phinney,^{1,2} X. Chen,^{4,5} S. D. Wilson,⁵ G. Cao,⁶ R. D. Averitt,³ G. Refael,^{1,2} and D. Hsieh^{1,2,*}

¹*Department of Physics, California Institute of Technology, Pasadena, CA 91125, USA*

²*Institute for Quantum Information and Matter,*

California Institute of Technology, Pasadena, CA 91125, USA

³*Department of Physics, University of California, San Diego, La Jolla, California 92093, USA*

⁴*Department of Physics, Boston College, Chestnut Hill, MA, 02467, USA*

⁵*Materials Department, University of California, Santa Barbara, CA, 93106, USA*

⁶*Department of Physics, University of Colorado, Boulder, CO 80309, USA*

(Dated: December 17, 2021)

Dynamically driven interacting quantum many-body systems have the potential to exhibit properties that defy the laws of equilibrium statistical mechanics. A widely studied model is the impulsively driven antiferromagnetic (AFM) Mott insulator, which is predicted to realize exotic transient phenomena including dynamical phase transitions into thermally forbidden states [1–3] and highly non-thermal magnon distributions [4]. However such far-from-equilibrium regimes, where conventional time-dependent Ginzburg-Landau descriptions fail, are experimentally challenging to prepare and to probe especially in solid state systems. Here we use a combination of time-resolved second harmonic optical polarimetry and coherent magnon spectroscopy to interrogate n -type photo-doping induced ultrafast magnetic order parameter (MOP) dynamics in the Mott insulator Sr_2IrO_4 . We find signatures of an unusual far-from-equilibrium critical regime in which the divergences of the magnetic correlation length and relaxation time are decoupled. This violation of conventional thermal critical behavior arises from the interplay of photo-doping and non-thermal magnon population induced demagnetization effects. Our findings, embodied in a non-equilibrium “phase diagram”, provide a blueprint for engineering the out-of-equilibrium properties of quantum matter, with potential applications to terahertz spintronics technologies.

The low energy electronic structure of the strongly spin-orbit coupled Mott insulator Sr_2IrO_4 consists of a completely filled band of spin-orbital entangled pseudospin $J_{\text{eff}} = 3/2$ states and a narrow half-filled band of $J_{\text{eff}} = 1/2$ states, which splits into lower and upper Hubbard bands due to on-site Coulomb repulsion [5]. Short-range AFM correlations between $J_{\text{eff}} = 1/2$ moments within a layer are established well above room temperature [6, 7]. But owing to weak interlayer exchange coupling ($J_c < 10^{-3}J_{ab}$) [7, 8], three-dimensional (3D) long-range AFM ordering only occurs below a Néel tem-

perature $T_N = 230$ K. The ordered structure exhibits a weak in-plane ferromagnetic moment in each layer due to pseudospin canting, which is staggered along the c -axis (Fig. 1a). Resonant x-ray and neutron scattering measurements of La-doped Sr_2IrO_4 have shown that a small concentration of n -type carriers destroys c -axis ordering, leaving behind a paramagnetic state with short-range 2D AFM correlations [9–11]. As such, n -type photo-doping, which may be simulated by optically pumping electrons from the electronically inert $J_{\text{eff}} = 3/2$ band into the upper Hubbard band, provides a potential pathway to impulsively quench long-range AFM order.

Recently, both ultrafast optical and free-electron laser-based resonant x-ray scattering (RXS) methods have been used to probe photo-doping induced pseudospin dynamics in iridates [12–16]. In the case of Sr_2IrO_4 , one study showed that it could be made magneto-optically active by aligning the canted moments in an external magnetic field [14]. Transient magnetization dynamics were then probed in the near-equilibrium weak photo-doping limit using time-resolved magneto-optical Kerr effect (MOKE) spectroscopy. The recovery time of the MOP was observed to diverge at T_N , which was explained within a time-dependent Ginzburg-Landau framework. In another pair of studies, time-resolved RXS was used to probe MOP dynamics without a field in a far-from-equilibrium strong photo-doping regime [12, 13]. A non-thermal melting of the MOP was achieved, but no critical dynamics were resolved across this phase transition.

The behavior of a system near a dynamical phase boundary should be sensitive to small changes in excitation density. In order to resolve out-of-equilibrium critical dynamics, it is therefore imperative that the excitation density be uniform throughout the probed volume and finely sampled near the phase boundary. Since the pump excitation density invariably decays with depth into the sample, one should in principle probe exclusively within a small interval of depth to minimize the effects of averaging over different excitation densities, which might otherwise obscure features of criticality (see Supplementary sections S1 and S2).

This condition is well met using an optical second harmonic generation rotational anisotropy (SHG-RA) technique (Fig. 1b), which was recently shown to be directly

* Corresponding author: dhsieh@caltech.edu

sensitive to the MOP in the topmost layer of Sr_2IrO_4 in zero magnetic field [17, 18]. We note that while an additional hidden order has been reported in Sr_2IrO_4 [19, 20], there is no indication that SHG couples to any hidden order [18], contrary to a previous interpretation [21]. In an SHG-RA experiment, light is focused obliquely onto the (001) face of Sr_2IrO_4 and the intensity of light reflected at twice the incident frequency $I(2\omega)$ is measured as the scattering plane is rotated about the surface normal. In equilibrium, SHG-RA patterns acquired above T_N exhibit four-fold (C_4) rotational symmetry, arising from a bulk electric-quadrupole (EQ) radiation from its centrosymmetric crystallographic point group [18]. Below T_N , an additional surface magnetization-induced electric-dipole (ED) contribution turns on and interferes with the EQ contribution, lowering the symmetry of the SHG-RA pattern from C_4 to C_1 (Fig. 1c).

To study the effects of n -type photo-doping, we developed time-resolved pump-probe SHG-RA using the apparatus depicted in Figure 1b. The pump beam, which was tuned on resonance with the $J_{\text{eff}} = 3/2$ band to upper Hubbard band transition, and probe beam were focused within a single magnetic domain for our experiments. Figure 1d shows transient SHG-RA data acquired at the instant of pump excitation ($t = 0$) as a function of pump fluence (F). In the un-pumped case ($F = 0$), the C_1 symmetry of the SHG-RA pattern is manifested through the presence of a dominant intensity lobe, indicating a finite ED contribution and thus a finite MOP. As F increases, the intensity of the dominant lobe decreases linearly until it plateaus above a critical fluence $F_c \approx 0.9 \text{ mJ/cm}^2$. Beyond F_c , the non-magnetic C_4 symmetry is fully restored to the SHG-RA pattern, signaling a collapsed MOP. The slightly higher C_4 -EQ yield from the pump-induced compared to heating-induced non-magnetic state likely arises from un-relaxed bulk magneto-elastic deformations that will be discussed in more detail below. The prompt change in the SHG-RA pattern within the time resolution of our instrument ($< 200 \text{ fs}$) for all fluences is consistent with a photo-doping scenario. Specifically, AFM order is suppressed by magnetic defects that are left in the wake of propagating doublons (Fig. 1b), which are generated on the time scale of the nearest-neighbor hopping ($< 20 \text{ fs}$) [14, 22, 23]. Moreover, the observed critical fluence corresponds to an excitation density (n_{ex}) of approximately 0.05 per iridium site, which is close to the reported critical La-doping level to suppress AFM order [9, 10], suggestive of an optical n -type doping induced quench mechanism.

More detailed comparisons between the properties of Sr_2IrO_4 in and out-of-equilibrium can be made by mapping the fluence versus temperature magnetic “phase diagram”. This is accomplished by collecting an array of SHG-RA patterns immediately after optical excitation across different starting temperatures and pump fluences and then tracking the onset of the ED contribution. For $F = 0$, the ED contribution emerges below T_N as expected (Fig. 2a). With increasing F , this transition

shifts monotonically to lower temperatures, indicating that F_c increases upon cooling. By plotting T_N as a function of n_{ex} , or equivalently F_c as a function of T , a sharp out-of-equilibrium magnetic phase boundary is identified. Despite an instantaneous electronic temperature that already far exceeds T_N at $F \approx 0.2 \text{ mJ/cm}^2$ based on the electronic specific heat of Sr_2IrO_4 (see Supplementary section S3), the photo-doping and La-doping phase boundaries nearly coincide over the small La-doping range where AFM order exists in equilibrium [9, 10] (Fig. 2b). This indicates that heat transfer from the charge to pseudospin subsystem is negligible near $t = 0$. Since chemical doping differs from photo-doping in non-trivial ways, including the introduction of disorder that is known to nucleate non-magnetic metallic puddles in La-doped Sr_2IrO_4 [9, 24], we refrain from drawing more detailed comparisons.

At later time delays, the charge, pseudospin and lattice subsystems are typically expected to thermalize and thus the out-of-equilibrium phase diagrams mapped at $t \approx 0$ and $t \gg 0$ should be different. Figure 2c shows the intensity of the dominant SHG-RA lobe over a range of fluence values, converted into effective temperatures using the total specific heat of Sr_2IrO_4 (see Methods), acquired at $t = 10 \text{ ps}$, which far exceeds the reported charge and lattice relaxation timescales but is much shorter than the timescale for heat to escape the probed region [23, 25]. At low fluences we find excellent agreement with the un-pumped temperature dependence data, confirming a pure optical heating effect. Surprisingly however, there is increasing bifurcation of the curves above $F \approx 0.8 \text{ mJ/cm}^2$, leading to a growing mismatch between the out-of-equilibrium phase boundary mapped at $t = 10 \text{ ps}$ and that calculated assuming pure optical heating as a function of fluence (Fig. 2d). This indicates that thermalization of the pseudospin subsystem is impeded at high fluences.

A hallmark of the La-doping induced paramagnetic state is the persistence of short-range intralayer AFM correlations, manifested through remnant dispersive 2D magnons detected by resonant inelastic x-ray scattering [10, 11]. To search for similar intralayer correlations in the photo-induced paramagnetic phase of Sr_2IrO_4 , we leverage the fact that the zone center 2D magnon mode with B_{2g} symmetry is weakly gapped ($\approx 2 \text{ meV}$) and Raman active [26, 27]. This allows the magnon to be coherently excited by our pump pulse via impulsive stimulated Raman scattering and optically tracked in the time domain using ultrafast MOKE spectroscopy [28]. Figures 2e,f show typical SHG and MOKE transients acquired in the high pump fluence ($F \gg F_c$) regime. Despite the complete collapse of the MOP over the displayed 10 ps time window (Fig. 2e), coherent oscillations of the infinite wavelength B_{2g} magnon continue to be supported (Fig. 2f). This provides clear evidence of a significant 2D magnetic correlation length in the transient paramagnetic state, suggesting a non-thermal analogue of La-doped Sr_2IrO_4 is realized. These results are consistent

with and complementary to a time-resolved RXS study of Sr_2IrO_4 [12], which showed that photo-doping strongly suppresses an AFM Bragg peak but does not alter the main high energy and short wavelength features of the intralayer magnon spectrum (see Supplementary section S4).

Having comprehensively mapped the transient magnetic phase diagram of Sr_2IrO_4 , we now finely examine the out-of-equilibrium critical dynamics. Figures 3a,b show the time-dependent change in intensity $\Delta I(2\omega)$ of the dominant SHG-RA lobe acquired at $T = 80$ K over a range of pump fluences. For $F \ll F_c$ (Fig. 3a), we observe a rapid drop in $\Delta I(2\omega)$ at $t = 0$ signifying a reduction of the MOP. This is followed by an exponential recovery with rise time $\tau \approx 1\text{--}2$ ps towards a value negatively offset from the $t < 0$ intensity, which we showed (Fig. 2c,d) represents a thermalized state with a slightly elevated temperature. As F increases, τ rises slightly but exhibits no discontinuity at F_c despite the MOP vanishing. However as F exceeds F_c , the point where C_4 symmetry is restored, τ continues to grow and eventually diverges around $F^* \approx 1.6$ mJ/cm² (Fig. 3b,c). Similar dynamics are observed if instead F is kept fixed and T is varied (inset Fig. 3a). These data reveal that the divergence of the magnetic correlation length and relaxation time occur along separated critical lines in the out-of-equilibrium phase diagram marked by F_c and F^* respectively (inset Fig. 3c). Such a decoupling is forbidden in equilibrium and is also not observed across dynamical phase transitions in weakly correlated ferromagnets [29] and charge density wave systems [30].

We note the presence of a subtle exponential drop just after $t = 0$ that becomes more pronounced at large F . This causes $\Delta I(2\omega)$ to drop below the instantaneous EQ value (gray bar in Fig. 1 and Figs. 3a,b and ultimately plateau at the high temperature EQ value upon reaching F^* . Given that magneto-elastic deformations are known to occur below T_N in Sr_2IrO_4 [8] and can cause small changes in the EQ response, a possible origin of this exponential component is lattice relaxation following impulsive suppression of the MOP. Therefore, only at large F when τ sufficiently exceeds the relevant phonon timescales do the magneto-elastic deformations have time to fully relax (see Supplementary section S5). Although

a direct confirmation awaits time-resolved crystallography measurements, the main conclusions of our work are independent of this interpretation.

To check whether the divergence of τ simply results from a prolonged photo-dopant lifetime, we performed simultaneous transient linear reflectivity ($\Delta R/R$) and SHG-RA measurements below T_N to directly compare the charge and pseudospin dynamics. As shown in Figures 4a-c, the generation of photo-dopants and their subsequent suppression of the MOP both occur within the time resolution of our experiment. However, unlike the SHG response, we observe no saturation in the amplitude of $\Delta R/R$ and no significant change in its characteristic recovery time ($\tau_0 \approx 1$ ps) as a function of fluence (inset Fig. 4a), demonstrating that the slow dynamics observed at F^* occur exclusively in the pseudospin sector. This suggests that τ must be governed by the relaxation of excess magnons that are emitted upon doublon decay. One possibility is that the magnons rapidly thermalize to a higher temperature and that τ represents the timescale for the hot pseudospin subsystem to cool via heat exchange with the lattice and charge subsystems. However, a three-temperature model describing this process predicts that magnons should cool faster at higher excitation densities. Moreover, it fails to produce any diverging timescale (see Supplementary sections S3 and S6). This points to the alternative possibility that τ represents the timescale for the pseudospin subsystem to internally thermalize.

The rate-limiting step for recovering long-range magnetic order is the establishment of c -axis correlations (Fig. 2e,f). Therefore τ must be set by the thermalization time of interlayer c -axis magnons. However the large mismatch between J_c (≈ 10 μeV) [7, 8] and both the charge gap (≈ 250 meV) [31] and lowest optical phonon energy (≈ 10 meV) [27] of Sr_2IrO_4 should impede c -axis magnon thermalization via charge or phonon excitation processes, leaving magnon-magnon scattering as the dominant thermalization channel. Building on the seminal work of Hohenberg and Halperin [32], we study the critical dynamics after doublon decay of this effectively closed c -axis magnon subsystem via a general stochastic Langevin equation for a real order parameter in one spatial dimension (see Supplementary section S7):

$$\partial_t \varphi_k(t) = -\left(k^2 + \tau_0^{-1}\right) \varphi_k(t) - \lambda \int \frac{dk_1}{2\pi} \int \frac{dk_2}{2\pi} \varphi_{k_1}(t) \varphi_{k_2}(t) \varphi_{k-k_1-k_2}(t) + \xi_k(t) \quad (1)$$

where $\varphi_k(t)$ is the k -th Fourier component of the MOP field $\varphi(z, t)$ that parameterizes the ordering of the intralayer Néel vector along the c -axis (Fig. 4d), τ_0^{-1} is a temperature-dependent mass term that is equivalent to the thermalization rate in a linearized Boltzmann equation [33], and λ parameterizes the interaction between magnons. Going beyond conventional time-dependent

Ginzburg-Landau descriptions, we introduce a Gaussian noise term $\xi_k(t)$ with $\langle \xi_k(t) \xi_{k'}(t') \rangle = \delta(t - t') \delta(k + k') (k^2 + \tau_0^{-1}) [2n_k(t) + 1]$ that imprints a non-equilibrium fluctuation-dissipation relation for some general magnon distribution function $n_k(t)$, in which the modes transverse to the c -axis are assumed to relax much faster and are thus integrated out [34]. To leading order, the equa-

tion of motion for the MOP $\Phi(t) = \langle \varphi_{k=0}(t) \rangle$ is given by $\partial_t \Phi(t) = -\tau^{-1} \Phi(t) - \lambda \Phi(t)^3$, and the Boltzmann equation for the magnon distribution is given by $\partial_t n_k(t) = -|\tau^{-1}| [n_k(t) - n_k^T]$, where $\tau^{-1} = \tau_0^{-1} - \lambda N_{\text{mag}}$ and n_k^T is the Bose distribution function corresponding to the final equilibrated magnon temperature T . These equations show that, in a closed system, the rate at which the MOP recovers to its equilibrium value at T via magnon thermalization is a decreasing function of the total number of excited magnons (N_{mag}). This provides an explanation for all key features of the data in Fig. 3c. In the low pump fluence limit where $N_{\text{mag}} \ll 1/\tau_0 \lambda$, τ approaches a lower bound that is naturally set by the photo-dopant decay time τ_0 . As N_{mag} grows with fluence, τ exhibits a power law increase following the reduced curvature of the Mexican hat potential. Finally once N_{mag} reaches $1/\tau_0 \lambda$ at the critical fluence F^* , τ diverges even though the total energy of the magnetic subsystem remains sub-critical (see Supplementary section S7). For $F \geq F^*$, thermalization can still eventually occur through the weak coupling between c -axis magnons and phonons, which is likely responsible for the slow (> 100 ps) MOP recovery observed by time-resolved RXS measurements at high fluences [12, 13]. Ultimately, on even longer timescales, the system cools back to the initial temperature via heat diffusion out of the pumped region (Fig. 4d).

Altogether, our results provide experimental signatures that static and dynamic critical behavior can be decoupled in a Mott antiferromagnet upon driving due to a subtle interplay of photo-doping and magnon thermalization processes (Fig. 4d). The hierarchy of magnetic, phononic and charge gap energy scales that enables this behavior in Sr_2IrO_4 is typical for layered transition metal oxide based AFM Mott insulators including the high- T_c superconducting cuprates, suggesting that our reported phenomena may be operational in numerous layered quantum materials. This raises the intriguing prospect of fine-tuning parameters such as τ_0 , F_c and F^* to optimize desired out-of-equilibrium properties. For example, extending τ_0 may be a pathway for realizing metastable electronic instabilities in a photo-doped Mott insulator, while the combination of a small τ_0 and F_c with a large F^* would be favorable for low-power high-speed AFM switching applications.

I. ACKNOWLEDGEMENTS

We thank L. Balents, A. Cavalleri, S. K. Cushing, E. Demler, S. Di Matteo, M. Endres, B. Fine, N. Gedik, D. Kennes, O. Mehio, H. Ning, M. Norman and M. Sentef for useful discussions. This work is supported by ARO MURI Grant No. W911NF-16-1-0361. D.H. also acknowledges support for instrumentation from the David and Lucile Packard Foundation and from the Institute for Quantum Information and Matter (IQIM), an NSF Physics Frontiers Center (PHY-1733907). A.d.l.T. acknowledges support from the Swiss National Science

Foundation through an Early Postdoc Mobility Fellowship (P2GEP2165044). M.B. acknowledges support from the Alexander von Humboldt foundation. N.J.L. acknowledges support from an IQIM Fellowship. G.C. acknowledges NSF support via a grant DMR-1712101.

II. COMPETING INTERESTS

The authors declare no competing interests.

III. METHODS

A. Sample growth

Single crystals of Sr_2IrO_4 were grown using a self-flux technique from off-stoichiometric quantities of IrO_2 , SrCO_3 and SrCl_2 . The ground mixtures of powders were melted at 1470°C in partially capped platinum crucibles. The soaking phase of the synthesis lasted for > 20 hours and was followed by a slow cooling at 2°C/hr to reach 1400°C . From this point the crucible is brought to room temperature through a rapid cooling at a rate of 100°C/hr . Crystals were cleaved along the (001) face just prior to measurements and immediately pumped down to a pressure $< 5 \times 10^{-6}$ torr in an optical cryostat.

B. Time-resolved spectroscopic probes

Time-resolved SHG-RA: Experiments were performed by splitting light from a regeneratively amplified Ti:sapphire laser, which produces 100 fs pulses with central wavelength $\lambda = 800$ nm at a repetition rate of 100 kHz, into pump and probe arms. The pump beam feeds an optical parametric amplifier, whose 1400 nm output beam is linearly polarized and sent through a delay line before being focused at normal incidence onto a $90 \mu\text{m}$ spot (FWHM) located within a single magnetic domain of a Sr_2IrO_4 crystal. As shown in Fig. 1b, the circularly polarized probe laser pulse ($\lambda = 800$ nm) traverses a linear input polarizer, phase mask and collimating lens and is focused at oblique incidence ($\approx 10^\circ$) onto a $30 \mu\text{m}$ spot within the pumped sample area using an objective lens. The reflected SHG pulse ($\lambda = 400$ nm) is re-collimated by the objective lens, linearly polarized by an output polarizer and then deflected onto a CCD camera by a triad of dichroic mirrors, which measures the SHG intensity at a fixed time delay with respect to the pump. The probe fluence was fixed to 1.5 mJ/cm^2 . A complete instantaneous SHG-RA pattern is acquired by mechanically co-rotating the input polarizer, phase mask and output polarizer, which implements a rotation of the probe scattering plane about the sample surface normal, and then projecting the SHG light reflected at each scattering plane angle onto different positions along a circular locus of points on the CCD camera [see Ref. [35] for

further details]. The procedure for converting raw CCD data to the polar SHG-RA plots shown in the main text is described in the Supplementary section S8. The SHG dynamics shown in Fig. 3 were reproduced under different polarization geometries and different scattering plane angles as shown in Supplementary section S9.

Time-resolved linear reflectivity: Transient reflectivity measurements were performed using exactly the same setup as that used for time-resolved SHG-RA as described above. Identical experimental conditions were preserved for the reflectivity and SHG-RA measurements, with the only change between experimental runs being the spectral filtering optics before the CCD camera to either isolate the 800 nm or 400 nm output.

Time-resolved MOKE: Experiments were performed by splitting light from a regeneratively amplified Ti:sapphire laser (repetition rate 1 kHz; pulse energy 6 mJ; pulse duration 100 fs; central wavelength $\lambda = 800$ nm) into pump and probe arms. The pump arm feeds a collinear dual-stage optical parametric amplifier, whose 1300 nm output beam is circularly polarized and then focused onto the sample at normal incidence. The probe arm ($\lambda = 800$ nm) is linearly S-polarized and focused near normal incidence onto the sample. To measure the polarization rotation (Kerr) angle of the reflected probe light, the reflected probe beam is sent through a half wave plate followed by a Wollaston prism. These optics are oriented such that in the absence of a pump beam ($\theta_k = 0$, $F = 4.6$ mJ/cm²), two equally intense beams of orthogonal linear polarization are produced, which are fed into the two input channels of a balanced photo-detector.

C. Conversion from F to n_{ex}

The number of photo-excitations n_{ex} created by the pump beam was calculated using the following equation:

$$n_{\text{ex}} = \frac{F(1-R)V_{\text{u.c.}}}{N_{\text{Ir}}E_{\text{ph}}\delta} \quad (2)$$

where F is the pump fluence, $R = 0.2$ and $\delta = 100$ nm are the sample reflectivity and penetration depth respectively at the pump wavelength $\lambda = 1400$ nm [36, 37], $V_{\text{u.c.}}$ is the unit cell volume of Sr₂IrO₄, N_{Ir} is the number of Ir atoms per unit cell, and E_{ph} the pump photon energy (0.89 eV).

D. Exponential fitting procedure for linear reflectivity

Transient linear reflectivity curves were fit to a double exponential function of the form $\Delta R/R = Ae^{-t/\tau_0} + Be^{-t/\tau_1} + C$. A high quality of fit is achieved as shown in Fig. 4a. The timescales extracted for τ_0 (≈ 1 ps) and τ_1 (≈ 200 fs) agree with the two exponential timescales associated with the decay of photo-induced midgap states observed by ultrafast angle-resolved photoemission spectroscopy measurements [23], attributed to acoustic phonon and optical phonon mediated photo-carrier relaxation processes respectively. Since the rate limiting step for photo-carrier relaxation is τ_0 , that is what we plot in the inset of Fig. 4a. We note that Ref. [23], also reported an absence of any fluence dependence for τ_0 , which is consistent with our observations (inset Fig. 4a).

-
- [1] Philipp Werner, Naoto Tsuji, and Martin Eckstein, “Nonthermal symmetry-broken states in the strongly interacting Hubbard model,” *Phys. Rev. B* **86**, 205101 (2012).
- [2] Matteo Sandri and Michele Fabrizio, “Nonequilibrium dynamics in the antiferromagnetic Hubbard model,” *Phys. Rev. B* **88**, 165113 (2013).
- [3] Naoto Tsuji, Martin Eckstein, and Philipp Werner, “Nonthermal Antiferromagnetic Order and Nonequilibrium Criticality in the Hubbard Model,” *Phys. Rev. Lett.* **110**, 136404 (2013).
- [4] Nicklas Walldorf, Dante M. Kennes, Jens Paaske, and Andrew J. Millis, “The antiferromagnetic phase of the Floquet-driven Hubbard model,” *Phys. Rev. B* **100**, 121110(R) (2019).
- [5] B. J. Kim, Hosub Jin, S. J. Moon, J.-Y. Kim, B.-G. Park, C. S. Leem, Jaehun Yu, T. W. Noh, C. Kim, S.-J. Oh, J.-H. Park, V. Durairaj, G. Cao, and E. Rotenberg, “Novel $J_{\text{eff}} = 1/2$ Mott State Induced by Relativistic Spin-Orbit Coupling in Sr₂IrO₄,” *Phys. Rev. Lett.* **101**, 076402 (2008).
- [6] S. Fujiyama, H. Ohsumi, T. Komesu, J. Matsuno, B. J. Kim, M. Takata, T. Arima, and H. Takagi, “Two-Dimensional Heisenberg Behavior of $J_{\text{eff}}=1/2$ Isospins in the Paramagnetic State of the Spin-Orbital Mott Insulator Sr₂IrO₄,” *Phys. Rev. Lett.* **108**, 247212 (2012).
- [7] J. G. Vale, S. Boseggia, H. C. Walker, R. Springell, Z. Feng, E. C. Hunter, R. S. Perry, D. Prabhakaran, A. T. Boothroyd, S. P. Collins, H. M. Rønnow, and D. F. McMorrow, “Importance of XY anisotropy in Sr₂IrO₄ revealed by magnetic critical scattering experiments,” *Phys. Rev. B* **92**, 020406 (2015).
- [8] J. Porras, J. Bertinshaw, H. Liu, G. Khaliullin, N. H. Sung, J.-W. Kim, S. Francoual, P. Steffens, G. Deng, M. Moretti Sala, A. Efimenko, A. Said, D. Casa, X. Huang, T. Gog, J. Kim, B. Keimer, and B. J. Kim, “Pseudospin-lattice coupling in the spin-orbit Mott insulator Sr₂IrO₄,” *Phys. Rev. B* **99**, 085125 (2019).
- [9] Xiang Chen, Tom Hogan, D. Walkup, Wenwen Zhou, M. Pokharel, Mengliang Yao, Wei Tian, Thomas Z. Ward, Y. Zhao, D. Parshall, C. Opeil, J. W. Lynn, Vidya Madhavan, and Stephen D. Wilson, “Influence of electron doping on the ground state of (Sr_{1-x}La_x)₂IrO₄,”

- Phys. Rev. B **92**, 075125 (2015).
- [10] H. Gretarsson, N. H. Sung, J. Porras, J. Bertinshaw, C. Dietl, Jan A. N. Bruin, A. F. Bangura, Y. K. Kim, R. Dinnebier, Jungho Kim, A. Al-Zein, M. Moretti Sala, M. Krisch, M. Le Tacon, B. Keimer, and B. J. Kim, “Persistent Paramagnons Deep in the Metallic Phase of $\text{Sr}_{2-x}\text{La}_x\text{IrO}_4$,” Phys. Rev. Lett. **117**, 107001 (2016).
- [11] D. Pincini, J. G. Vale, C. Donnerer, A. de la Torre, E. C. Hunter, R. Perry, M. Moretti Sala, F. Baumberger, and D. F. McMorrow, “Anisotropic exchange and spin-wave damping in pure and electron-doped Sr_2IrO_4 ,” Phys. Rev. B **96**, 075162 (2017).
- [12] M. P. M. Dean, Y. Cao, X. Liu, S. Wall, D. Zhu, R. Mankowsky, V. Thampy, X. M. Chen, J. G. Vale, D. Casa, Jungho Kim, A. H. Said, P. Juhás, R. Alonso-Mori, J. M. Glowina, A. Robert, J. Robinson, M. Sikorski, S. Song, M. Kozina, H. Lemke, L. Patthey, S. Owada, T. Katayama, M. Yabashi, Yoshikazu Tanaka, T. Togashi, J. Liu, C. Rayan Serrao, B. J. Kim, L. Huber, C.-L. Chang, D. F. McMorrow, M. Först, and J. P. Hill, “Ultrafast energy- and momentum-resolved dynamics of magnetic correlations in the photo-doped Mott insulator Sr_2IrO_4 ,” Nature Materials **15**, 601–605 (2016).
- [13] O Krupin, G L Dakovski, B J Kim, J W Kim, Jungho Kim, S Mishra, Yi-De Chuang, C R Serrao, W-S Lee, W F Schlotter, M P Minitti, D Zhu, D Fritz, M Chollet, R Ramesh, S L Molodtsov, and J J Turner, “Ultrafast dynamics of localized magnetic moments in the unconventional Mott insulator Sr_2IrO_4 ,” Journal of Physics: Condensed Matter **28**, 32LT01 (2016).
- [14] D. Afanasiev, A. Gatilova, D. J. Groenendijk, B. A. Ivanov, M. Gibert, S. Gariglio, J. Mentink, J. Li, N. Dasari, M. Eckstein, Th. Rasing, A. D. Caviglia, and A. V. Kimel, “Ultrafast Spin Dynamics in Photodoped Spin-Orbit Mott Insulator Sr_2IrO_4 ,” Phys. Rev. X **9**, 021020 (2019).
- [15] Daniel G. Mazzone, Derek Meyers, Yue Cao, James G. Vale, Cameron D. Dashwood, Youguo Shi, Andrew J. A. James, Neil J. Robinson, Jiaqi Lin, Vivek Thampy, Yoshikazu Tanaka, Allan S. Johnson, Hu Miao, Ruitang Wang, Tadesse A. Assefa, Jungho Kim, Diego Casa, Roman Mankowsky, Diling Zhu, Roberto Alonso-Mori, Sanghoon Song, Hasan Yavas, Tetsuo Katayama, Makina Yabashi, Yuya Kubota, Shigeki Owada, Jian Liu, Junji Yang, Robert M. Konik, Ian K. Robinson, John P. Hill, Desmond F. McMorrow, Michael Först, Simon Wall, Xuerong Liu, and Mark P. M. Dean, “Laser-induced transient magnons in $\text{sr}_3\text{ir}_2\text{o}_7$ throughout the brillouin zone,” Proceedings of the National Academy of Sciences **118** (2021), 10.1073/pnas.2103696118.
- [16] Ernest Pastor, David Moreno-Mencía, Maurizio Monti, Allan S. Johnson, Nina Fleischmann, Cuixiang Wang, Youguo Shi, Xuerong Liu, Daniel G. Mazzone, Mark P. M. Dean, and Simon Wall, “Non-thermal breaking of magnetic order via photo-generated spin defects,” (2021), arXiv:2104.04294 [cond-mat.str-el].
- [17] S. Di Matteo and M. R. Norman, “Magnetic ground state of Sr_2IrO_4 and implications for second-harmonic generation,” Phys. Rev. B **94**, 075148 (2016).
- [18] K. L. Seyler, A. de la Torre, Z. Porter, E. Zoghlin, R. Polski, M. Nguyen, S. Nadj-Perge, S. D. Wilson, and D. Hsieh, “Spin-orbit-enhanced magnetic surface second-harmonic generation in Sr_2IrO_4 ,” Phys. Rev. B **102**, 201113 (R) (2020).
- [19] Jaehong Jeong, Yvan Sidis, Alex Louat, Véronique Brouet, and Philippe Bourges, “Time-reversal symmetry breaking hidden order in $\text{sr}_2(\text{ir},\text{rh})\text{o}_4$,” Nature Communications **8**, 15119 (2017).
- [20] H. Murayama, K. Ishida, R. Kurihara, T. Ono, Y. Sato, Y. Kasahara, H. Watanabe, Y. Yanase, G. Cao, Y. Mizukami, T. Shibauchi, Y. Matsuda, and S. Kasahara, “Bond directional anapole order in a spin-orbit coupled mott insulator $\text{sr}_2(\text{ir}_{1-x}\text{rh}_x)\text{o}_4$,” Phys. Rev. X **11**, 011021 (2021).
- [21] L. Zhao, D. H. Torchinsky, H. Chu, V. Ivanov, R. Lifshitz, R. Flint, T. Qi, G. Cao, and D. Hsieh, “Evidence of an odd-parity hidden order in a spin-orbit coupled correlated iridate,” Nature Physics **12**, 32–36 (2016).
- [22] Akira Takahashi, Hiroki Gomi, and Masaki Aihara, “Photoinduced superconducting states in strongly correlated electron systems,” Phys. Rev. B **66**, 115103 (2002).
- [23] C. Piovera, V. Brouet, E. Papalazarou, M. Caputo, M. Marsi, A. Taleb-Ibrahimi, B. J. Kim, and L. Perfetti, “Time-resolved photoemission of Sr_2IrO_4 ,” Phys. Rev. B **93**, 241114 (2016).
- [24] I. Battisti, K. M. Bastiaans, V. Fedoseev, A. de la Torre, N. Iliopoulos, A. Tamai, E. C. Hunter, R. S. Perry, J. Zanen, F. Baumberger, and M. P. Allan, “Universality of pseudogap and emergent order in lightly doped Mott insulators,” Nature Physics **13**, 21–25 (2017).
- [25] D. Hsieh, F. Mahmood, D. H. Torchinsky, G. Cao, and N. Gedik, “Observation of a metal-to-insulator transition with both Mott-Hubbard and Slater characteristics in Sr_2IrO_4 from time-resolved photocarrier dynamics,” Phys. Rev. B **86**, 035128 (2012).
- [26] Y. Gim, A. Sethi, Q. Zhao, J. F. Mitchell, G. Cao, and S. L. Cooper, “Isotropic and anisotropic regimes of the field-dependent spin dynamics in Sr_2IrO_4 : Raman scattering studies,” Phys. Rev. B **93**, 024405 (2016).
- [27] H. Gretarsson, J. Saucedo, N. H. Sung, M. Höppner, M. Minola, B. J. Kim, B. Keimer, and M. Le Tacon, “Raman scattering study of vibrational and magnetic excitations in $\text{Sr}_{2-x}\text{La}_x\text{IrO}_4$,” Phys. Rev. B **96**, 115138 (2017).
- [28] Urban F. P. Seifert and Leon Balents, “Optical excitation of magnons in an easy-plane antiferromagnet: Application to sr_2iro_4 ,” Phys. Rev. B **100**, 125161 (2019).
- [29] Phoebe Tengdin, Wenjing You, Cong Chen, Xun Shi, Dmitriy Zusin, Yingchao Zhang, Christian Gentry, Adam Blonsky, Mark Keller, Peter M. Oppeneer, Henry C. Kapteyn, Zhensheng Tao, and Margaret M. Murnane, “Critical behavior within 20 fs drives the out-of-equilibrium laser-induced magnetic phase transition in nickel,” Science Advances **4** (2018), 10.1126/sciadv.aap9744.
- [30] Alfred Zong, Pavel E. Dolgirev, Anshul Kogar, Emre Ergeçen, Mehmet B. Yilmaz, Ya-Qing Bie, Timm Rohwer, I-Cheng Tung, Joshua Straquadine, Xirui Wang, Yafang Yang, Xiaozhe Shen, Renkai Li, Jie Yang, Suji Park, Matthias C. Hoffmann, Benjamin K. Ofori-Okai, Michael E. Kozina, Haidan Wen, Xijie Wang, Ian R. Fisher, Pablo Jarillo-Herrero, and Nuh Gedik, “Dynamical slowing-down in an ultrafast photoinduced phase transition,” Phys. Rev. Lett. **123**, 097601 (2019).
- [31] A. de la Torre, S. McKeown Walker, F. Y. Bruno, S. Riccò, Z. Wang, I. Gutierrez Lezama, G. Scheerer, G. Giriat, D. Jaccard, C. Berthod, T. K. Kim, M. Hoesch, E. C. Hunter, R. S. Perry, A. Tamai, and F. Baumberger, “Collapse of the Mott Gap and Emergence of a Nodal

- Liquid in Lightly Doped Sr_2IrO_4 ,” *Phys. Rev. Lett.* **115**, 176402 (2015).
- [32] P. C. Hohenberg and B. I. Halperin, “Theory of dynamic critical phenomena,” *Rev. Mod. Phys.* **49**, 435–479 (1977).
- [33] L M Sieberer, M Buchhold, and S Diehl, “Keldysh field theory for driven open quantum systems,” *Reports on Progress in Physics* **79**, 096001 (2016).
- [34] Pavel E. Dolgirev, Marios H. Michael, Alfred Zong, Nuh Gedik, and Eugene Demler, “Self-similar dynamics of order parameter fluctuations in pump-probe experiments,” *Phys. Rev. B* **101**, 174306 (2020).
- [35] J. W. Harter, L. Niu, A. J. Woss, and D. Hsieh, “High-speed measurement of rotational anisotropy nonlinear optical harmonic generation using position-sensitive detection,” *Opt. Lett.* **40**, 4671–4674 (2015).
- [36] J. S. Lee, Y. Krockenberger, K. S. Takahashi, M. Kawasaki, and Y. Tokura, “Insulator-metal transition driven by change of doping and spin-orbit interaction in Sr_2IrO_4 ,” *Phys. Rev. B* **85**, 035101 (2012).
- [37] J. Nichols, O. B. Korneta, J. Terzic, L. E. De Long, G. Cao, J. W. Brill, and S. S. A. Seo, “Anisotropic electronic properties of a-axis-oriented Sr_2IrO_4 epitaxial thin-films,” *Applied Physics Letters* **103**, 131910 (2013).

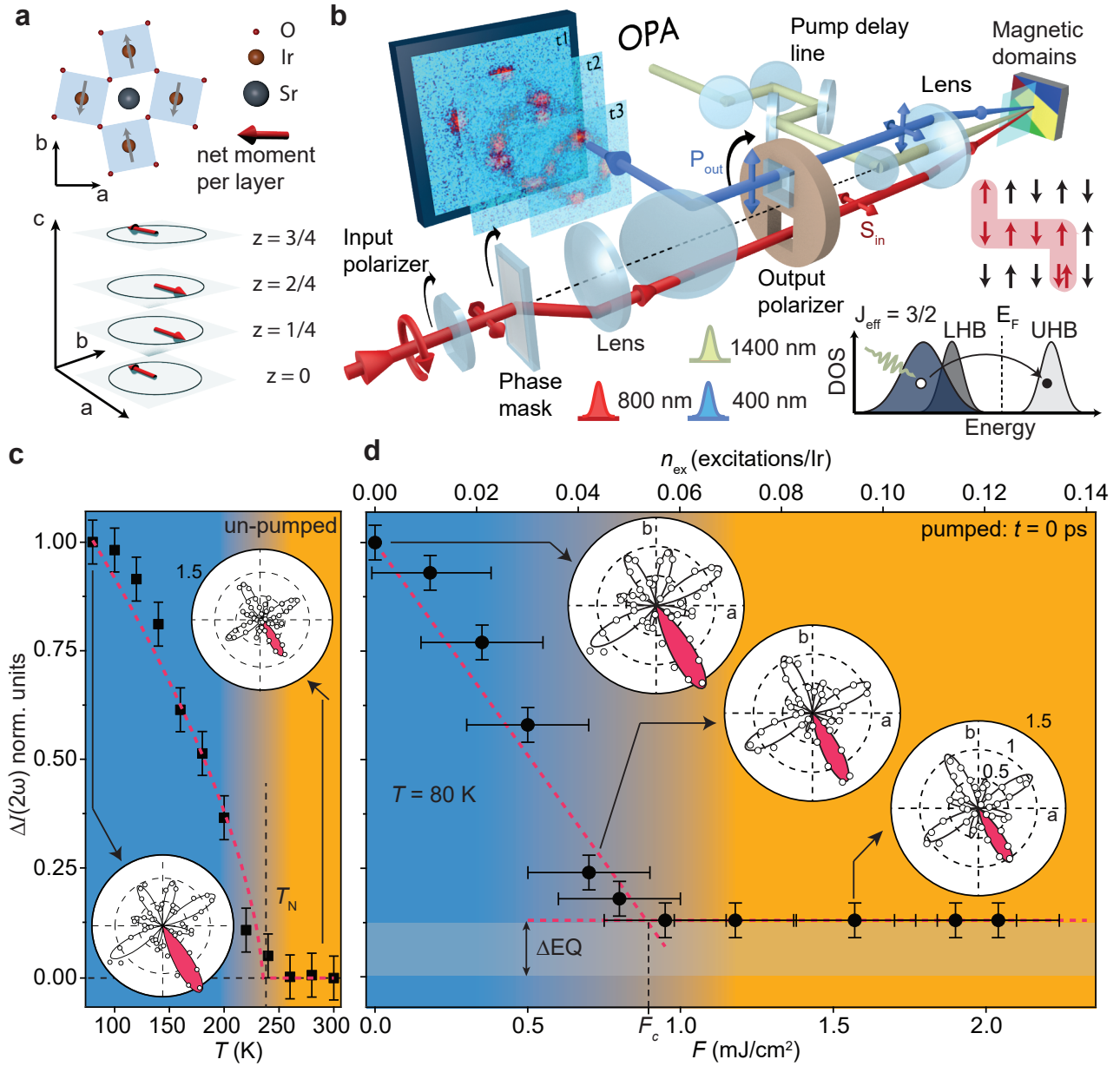


FIG. 1. Instantaneous photo-doping response of magnetic order in Sr_2IrO_4 . **a**, Intralayer magnetic order of Sr_2IrO_4 . Each layer possesses a non-zero net moment due to pseudospin canting, which are staggered along the c -axis. **b**, Schematic of the time-resolved SHG-RA setup. A circularly polarized probe laser pulse ($\lambda = 800$ nm) traverses a linear polarizer, phase mask, collimating lens and is focused onto the sample at oblique incidence using an objective lens. The reflected SHG pulse ($\lambda = 400$ nm) is re-collimated by the objective, linearly polarized and deflected onto a CCD camera by a dichroic mirror. Different scattering plane angles are accessed by mechanically co-rotating select optics. Data shown throughout the manuscript are acquired in the $P_{\text{in}}\text{-}S_{\text{out}}$ polarization channel (see Methods). A time-delayed linearly polarized pump pulse resonant with the $J_{\text{eff}} = 3/2$ to upper Hubbard band energy ($\lambda = 1400$ nm) is focused normally onto the sample. Regions of different color on the sample represent distinct magnetic domains identified by SHG imaging. Inset: schematic of doublon generation and propagation. **c**, Temperature dependence of the change in SHG intensity $\Delta I(2\omega)$ relative to $T = 300$ K for an un-pumped sample acquired at the angle of maximum intensity (pink). Dashed line is a guide to the eye. **d**, Pump fluence dependence of $\Delta I(2\omega)$ at $t = 0$ and $T = 80$ K with corresponding SHG-RA patterns. Fits to the data below (above) F_c including both EQ and ED terms (solely EQ term) are overlaid. Height of the gray bar represents the change in EQ SHG intensity with respect to the equilibrium value as discussed in the main text. Horizontal error bars represent the systematic error in calculating n_{ex} .

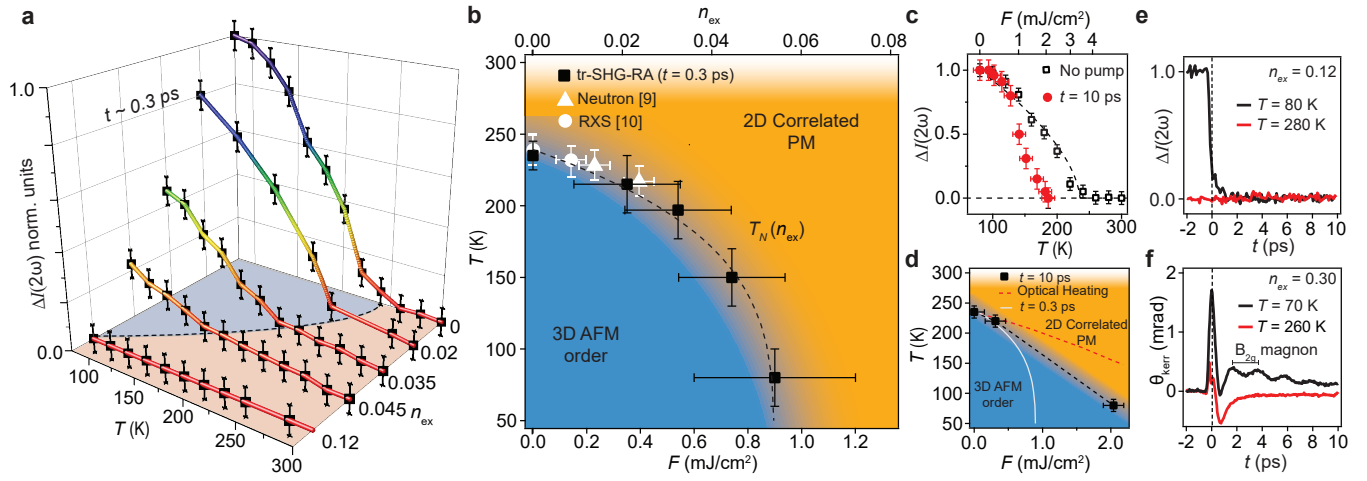


FIG. 2. Out-of-equilibrium magnetic phase diagrams. **a**, Temperature dependence of $\Delta I(2\omega)$ at $t = 0.3$ ps for select pump excitation densities n_{ex} and **b**, the out-of-equilibrium phase diagram mapped using such datasets (at $t = 0.3$ ps). The reported La-doping dependence of T_N is overlaid. Horizontal error bars represent the systematic error in calculating n_{ex} . **c**, Comparison of the temperature dependence of $\Delta I(2\omega)$ for an unpumped sample with the fluence dependence of $\Delta I(2\omega)$ collected at $t = 10$ ps and $T = 80$ K, where F is converted into an effective temperature by assuming all of the pump energy goes into quasi-equilibrium heating. **d**, The out-of-equilibrium phase diagram mapped at $t = 10$ ps (black dashed line). Overlaid are the phase boundary reproduced from panel **b** (white line) and that calculated assuming all of the pump energy goes into quasi-equilibrium heating (red line). **e**, High fluence $\Delta I(2\omega)$ and **f**, MOKE transients acquired below and above T_N .

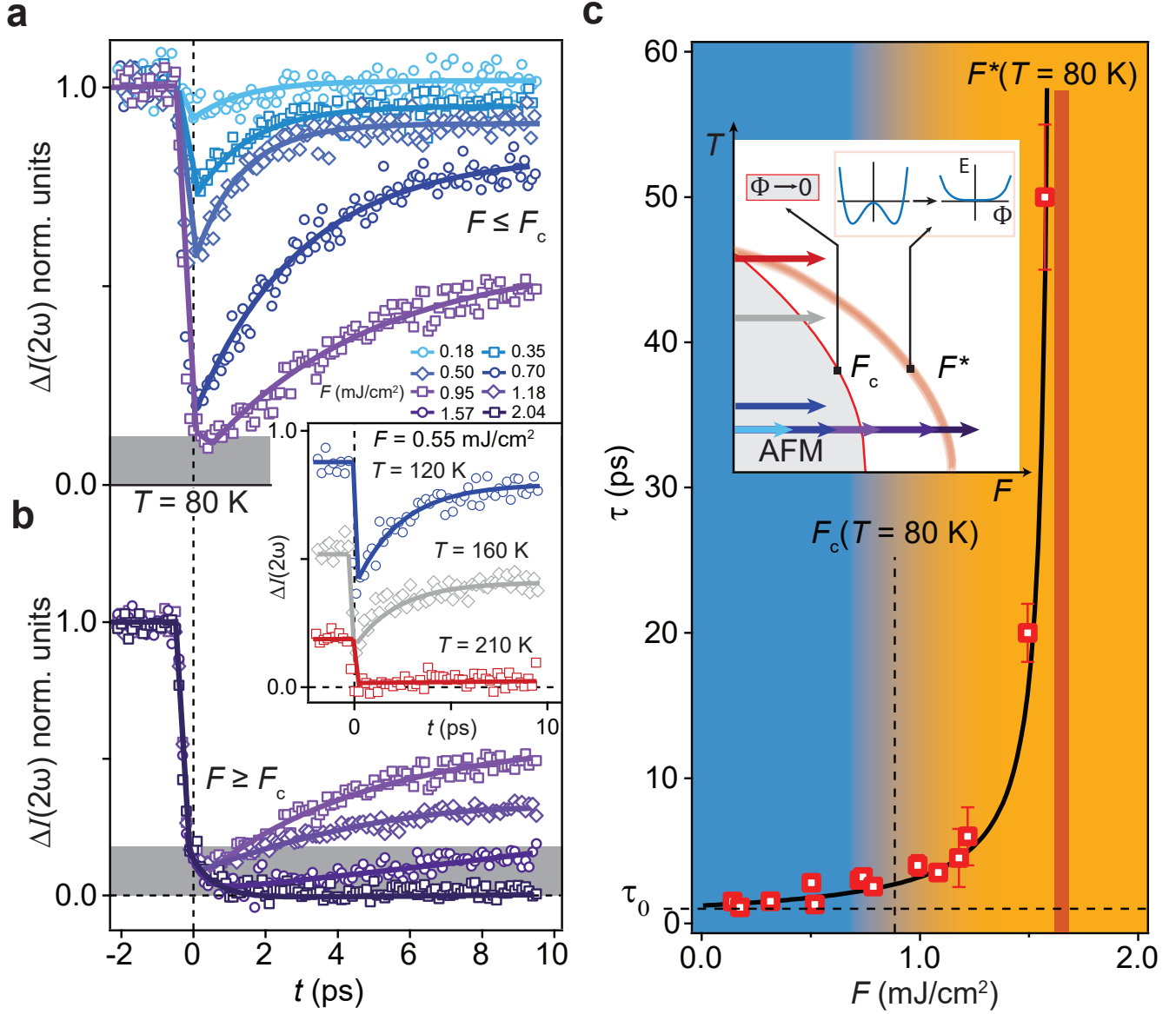


FIG. 3. **Out-of-equilibrium critical dynamics of the magnetic order parameter.** $\Delta I(2\omega)$ transients acquired at $T = 80$ K for select fluences **a**, below and **b**, above F_c . The height of the gray bar denotes the excess EQ SHG intensity at $t = 0$ as discussed in the main text. Inset shows analogous data acquired at fixed $F = 0.55$ mJ/cm² for different temperatures. Solid lines are fits of the recovery to a single exponential function plus a constant determined by the long time offset of the SHG intensity. **c**, Plot of fitted exponential relaxation times versus fluence superposed with a fit to the function $\tau = \tau_0(1 - F/F^*)^{-1}$, with τ_0 fixed to 1.2 ps by the transient reflectivity data (Fig. 4a). The values of F_c and F^* at $T = 80$ K based on the data in panels **a**, **b** and the fit (black line) respectively are explicitly marked. The decoupling of the divergence in magnetic correlation length (defined by F_c) from the divergence in relaxation time (defined by F^*) is illustrated in the inset based on the data in panels **a** and **b**. The arrows are color coded in correspondence to the curves in panels **a** and **b** and point to the location in the out-of-equilibrium phase diagram being accessed. Schematics show the the out-of-equilibrium free energy landscape after doublon decay based on the Langevin theory described in the text.

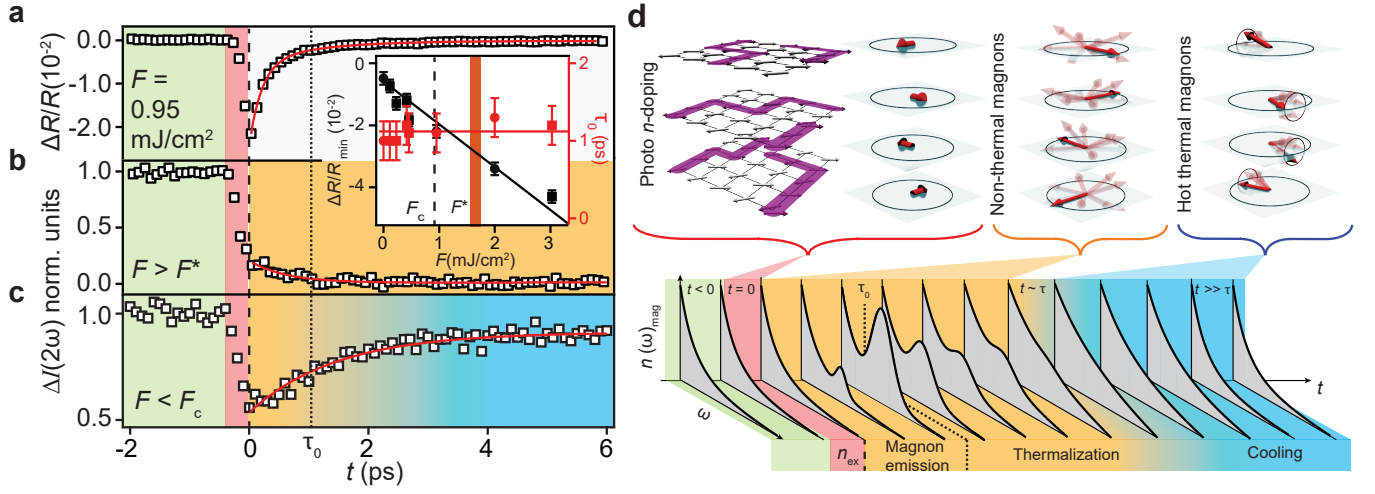


FIG. 4. **Magnon population induced critical slowing down.** Simultaneous measurements of the **a**, transient reflectivity and **b-c**, transient SHG intensity acquired under identical experimental conditions (except for fluence) at $T = 80$ K. Inset of panel **a**: fluence dependence of the intensity minimum and characteristic recovery time τ_0 extracted through double exponential fits (red curve) to the $\Delta R/R$ data (see Methods). **d**, Schematic of the complete temporal evolution of (top) the real space c -axis magnetic correlations and (bottom) the magnon distribution function $n(\omega)$ versus energy ω following pump excitation. Over the time window $0 < t \lesssim \tau$ (shaded orange), $n(\omega)$ departs from Bose-Einstein form.

Supplementary Information

Decoupling of static and dynamic criticality in a driven Mott insulator

A. de la Torre^{1,2}, K. L. Seyler^{1,2}, M. Buchhold^{1,2}, Y. Baum^{1,2}, G. Zhang³, N. J. Laurita^{1,2}, J. W. Harter^{1,2}, L. Zhao^{1,2}, I. Phinney^{1,2}, X. Chen^{4,5}, S. D. Wilson⁵, G. Cao⁶, R. D. Averitt³, G. Refael^{1,2} & D. Hsieh^{1,2}

¹*Department of Physics, California Institute of Technology, Pasadena, CA 91125, USA.*

²*Institute for Quantum Information and Matter, California Institute of Technology, Pasadena, CA 91125, USA.*

³*Department of Physics, University of California, San Diego, La Jolla, California 92093, USA*

⁴*Department of Physics, Boston College, Chestnut Hill, MA, 02467, USA*

⁵*Materials Department, University of California, Santa Barbara, CA, 93106, USA*

⁶*Center for Advanced Materials, Department of Physics and Astronomy, University of Kentucky, Lexington, Kentucky 40506, USA.*

Contents:

- S1. Effect of multiple layers on the measured magnetization dynamics**
- S2. Time-resolved SHG transients in the presence of a magnetic field**
- S3. Two- and three-temperature model results**
- S4. Coherent in-plane magnon in the $F > F_c$ regime**
- S5. Time-resolved SHG transients for $F > F^*$**
- S6. Ruling out alternative explanations for slow dynamics**
- S7. Details of the Langevin theory**
- S8. Restoration of the initial SHG-RA pattern after relaxation**
- S9. Time-resolved SHG transients for different polarization channels**

S1. Effect of multiple layers on the measured magnetization dynamics

In this section we simulate how time-resolved transients differ depending on whether the probe is sensitive exclusively to a single surface magnetic layer (as in our experiments) or to multiple magnetic layers below the surface.

Let the bulk magnetization be given by $\sum_i M_i$, where M_i is the magnetization of layer i normalized to 1. We assume the time dependence of the layer magnetization to be $M_i(t) = 1 - \Delta M_i(F_i)e^{-t/\tau(F_i)}$. Due to the finite penetration depth of the pump light, each layer experiences a different effective fluence $F_i = F(1 - R)e^{-z_i/\delta}$, where F is the applied fluence, $z_i = i \times c/4$ with $c = 2.58$ nm being the c -axis lattice constant, and $\delta = 100$ nm [1] and $R = 0.2$ [2] are respectively the penetration depth and reflectivity at the pump wavelength $\lambda = 1400$ nm. We assume that $\Delta M_i(F_i)$ and $\tau(F_i)$ follow the curves shown in Fig. 1d and Fig. 3c of the main text respectively.

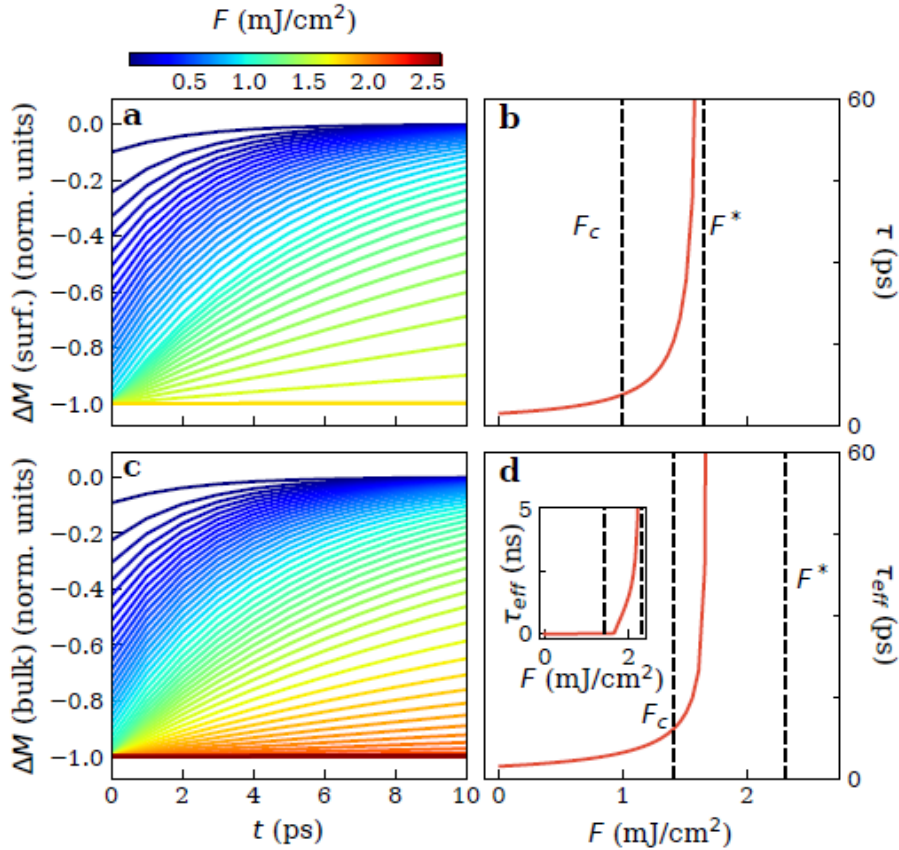


Figure S1: Simulated transient dynamics of **a**, the surface magnetization and **c**, the bulk magnetization for different applied pump fluences. **b** and **d** show the values of the relaxation constant τ extracted from fitting the curves in **a** and **b** respectively to a single exponential recovery. Vertical dashed lines indicate F_c and F^* for the surface and bulk. The inset in **d** shows the full range of τ_{eff} up to where it diverges at F^* . The sudden upturn around $F = 1.6$ mJ/cm^2 occurs where the fluence of the surface layer just reaches F^* .

The transient magnetization dynamics are computed using the expression $\Delta M(t) = [M(t) - M(t^{<0})]/M(t^{<0})$, where $M(t) = \sum_i M_i(t)$ and $M(t^{<0})$ is the pre-

time zero magnetization. For the surface magnetization calculation, we only retain the $i = 0$ term. Figures S1a and b show the fluence dependence of the simulated surface magnetization transients and the time constants extracted from fits to a single exponential, which follow the trends shown in Fig.3 of the main text by construction. For the bulk magnetization calculation, we restrict the sum to the first 48 layers (12 u.c.) to match the probe penetration depth at $\lambda = 400$ nm ($\delta = 31.25$ nm). As shown in Fig. S1c and d, there are some key differences with the surface dynamics. First, based on our calculations, the critical fluences F_c and F^* are larger for the bulk case than for the surface case by a factor of $e^{z_i/\delta}$ with $i = 48$ and $\delta = 100$ nm. Second, the effective time constant τ_{eff} extracted from fits to a single exponential function exhibits a steep increase with fluence just above F_c , in contrast to the surface case where the steep increase occurs well above F_c . This arises because at the point where F_c is reached throughout the bulk, the top layers already experience a fluence close to F^* and contribute slow exponential terms to the sum over i . This makes the separation between F_c and F^* more difficult to resolve in the bulk case, and serves as a motivation for using a surface sensitive probe.

S2. Time-resolved SHG transients in the presence of a magnetic field

Recent work [3] showed that when Sr_2IrO_4 is in the zero magnetic field $- + + -$ state, the SHG signal is dominated by a surface electric-dipole (ED) contribution. On the other hand, in an in-plane magnetic field $H > H_c = 200$ mT, there is a metamagnetic transition into a $+ + + +$ state [4], where the SHG signal becomes dominated by a bulk magnetization-induced magnetic-dipole (MD) contribution.

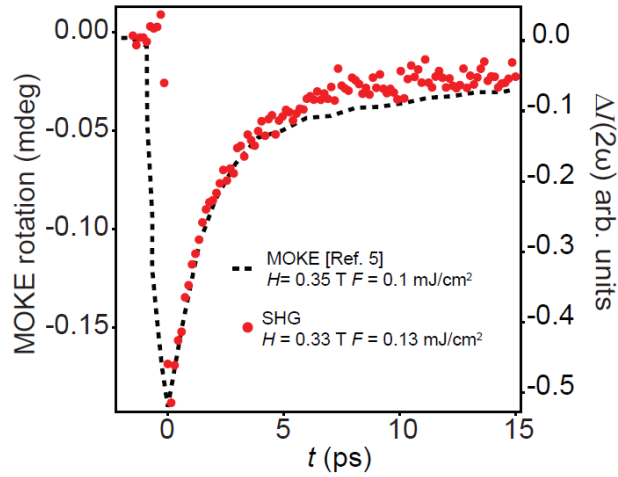


Figure S2. A comparison of in-field MOKE transients (adapted from Ref.[5]) and in-field SHG transients acquired under similar field and fluence.

We performed in-field ($H = 330$ mT) time-resolved SHG-RA measurements on Sr_2IrO_4 using the short working-distance magnetic microstat apparatus described in Ref. [3]. As shown in Fig. S2, the in-field SHG transient acquired in the low fluence regime undergoes a prompt suppression and exponential recovery, reminiscent of our zero-field data. This verifies that photo-excitation is suppressing magnetic order in the bulk and not exclusively at the surface. We note that the dynamics reported in a recent ultrafast MOKE study [5] performed in the low fluence regime $F < 0.3$ mJ/cm² agree very well with our in-field SHG results (Fig. S2), which further confirms that both techniques are probing the recovery of $+ + + +$ order with bulk sensitivity.

S3. Two- and three-temperature model results

Early pioneering work on laser-induced ultrafast demagnetization of ferromagnetic nickel introduced a three-temperature model (3TM) to explain its out-of-equilibrium dynamics [6]. This model assumes that immediately following photo-excitation, the electronic (e), lattice (l) and spin (s) subsystems form three thermalized reservoirs with independent temperatures and specific heats (C_e, T_e), (C_l, T_l) and (C_s, T_s), which interact via a set of coupling constants (g_{el} , g_{es} , g_{sl}) that control the rate of heat transfer between the different reservoirs. In such models, suppression of the magnetic ordering arises from a thermal effect related to an increase of T_s .

While such models are less applicable to insulating systems like Sr_2IrO_4 , we nevertheless performed a 3TM analysis using the set of coupled differential equations below to explicitly show that such thermal effects cannot explain our observations in Sr_2IrO_4 .

$$\begin{aligned} C_e(T_e) \frac{dT_e}{dt} &= -g_{el}(T_e - T_l) - g_{es}(T_e - T_s) \\ C_l(T_l) \frac{dT_l}{dt} &= g_{el}(T_e - T_l) - g_{ls}(T_l - T_s) \\ C_s(T_s) \frac{dT_s}{dt} &= g_{es}(T_e - T_s) + g_{ls}(T_l - T_s) \end{aligned}$$

The electronic heat capacity was taken to be $C_e = \gamma T_e$, with $\gamma = 2 \text{ mJ/mol K}^2$ [7], the lattice heat capacity was modelled using a sixth order polynomial fit to the reported data in Ref. [7] and the spin specific heat was assumed to take the form predicted for a 2D spin-1/2 Heisenberg antiferromagnet [8]. Heat diffusion away from the probed region was not included in our model because it is much slower than the equilibration processes of interest. We assume that the pump pulse acts to instantaneously raise only T_e by an amount:

$$T_e(t = 0) = \sqrt{\frac{2 * F * (1 - R)}{\delta * \gamma} + T_e(t < 0)^2}$$

where F is the pump fluence, $R = 0.2$ [1] and $\delta = 100 \text{ nm}$ [2] are the sample reflectivity and penetration depth at $\lambda = 1400 \text{ nm}$ respectively. Both T_l and T_s are assumed to remain at the pre-pumped equilibrium temperature at $t = 0$.

We assumed a value of $5 \times 10^{12} \text{ W/mol-K}$ for g_{el} , g_{sl} and g_{es} , which is reasonable for real materials [9], in order to account for the following experimentally known features of Sr_2IrO_4 : (i) There is substantial coupling between electronic, lattice and spin degrees of freedom within each Ir-O layer and so we treat them on equal footing; (ii) It produces a decay time of T_e consistent with the observed timescale of τ_0 ; (3) The system is fully equilibrated by $t = 10 \text{ ps}$ (at least for low fluences). We note that the relevant qualitative

trends exhibited by the 3TM (as described below) do not depend on the exact values chosen for g_{el} , g_{sl} and g_{es} . Therefore, choosing a different set of values would not affect our conclusions. Solutions to the two-temperature model (2TM) involving only T_e and T_l can be obtained by simply setting g_{es} and g_{sl} to zero in our 3TM, which exhibit qualitatively similar behaviour.

Figure S3 shows the solution of the 3TM using several representative values of the pump fluence and $T = 80$ K. The following key features show why it cannot explain our experiments:

- (i) T_e far exceeds T_N even for $F \ll F_c$, which indicates that the experimentally observed suppression of the MOP is not due to heating of the electronic subsystem.
- (ii) T_s begins to rise only after T_e begins to fall. This is not compatible with our observations in Fig. 4a-c of the main text, which show that charge excitation and suppression of the MOP occur concurrently within our resolution.
- (iii) There is no evidence for a slow relaxation timescale for T_s or any anomaly in its relaxation rate within the 3TM, even at high fluences where T_s crosses T_N . One can understand that this must be true simply by inspecting the equation governing the relaxation rate of T_s , namely $\frac{1}{c_s(T_s)} [g_{es}(T_e - T_s) + g_{ls}(T_l - T_s)]$. First, no divergence of C_s has been observed at T_N in specific heat measurements [7], which is naturally expected for Sr_2IrO_4 because T_N is merely the temperature where already in-plane correlated 2D planes become locked along the c -axis. Much of the magnetic entropy is already lost far above T_N where in-plane correlations develop. Second, the temperature differences $T_e - T_s$ and $T_l - T_s$ set a global scale for the system relaxation rate that cannot be erased by any internal dynamics of the magnons. Therefore, there is simply no mechanism for a diverging timescale in this model.
- (iv) Higher pump fluence leads to a higher relaxation rate of T_s for the reasons discussed above in (iii), which is opposite to the behavior observed for τ . Note that this effect will be even more pronounced in the time dependence of $\Delta I(2\omega)$ because of the form of the nonlinear conversion function between T_s and $\Delta I(2\omega)$ (Fig. 1c).
- (v) For fluence values where T_s begins to cross T_N (Fig. S3b), one would expect the ED SHG signal to be zero during the time interval where $T_s > T_N$. Once T_s dips back below T_N the ED SHG signal should recover very fast because the SHG intensity is a steep function of temperature just below T_N . Such discontinuous features are not observed in our experiments.

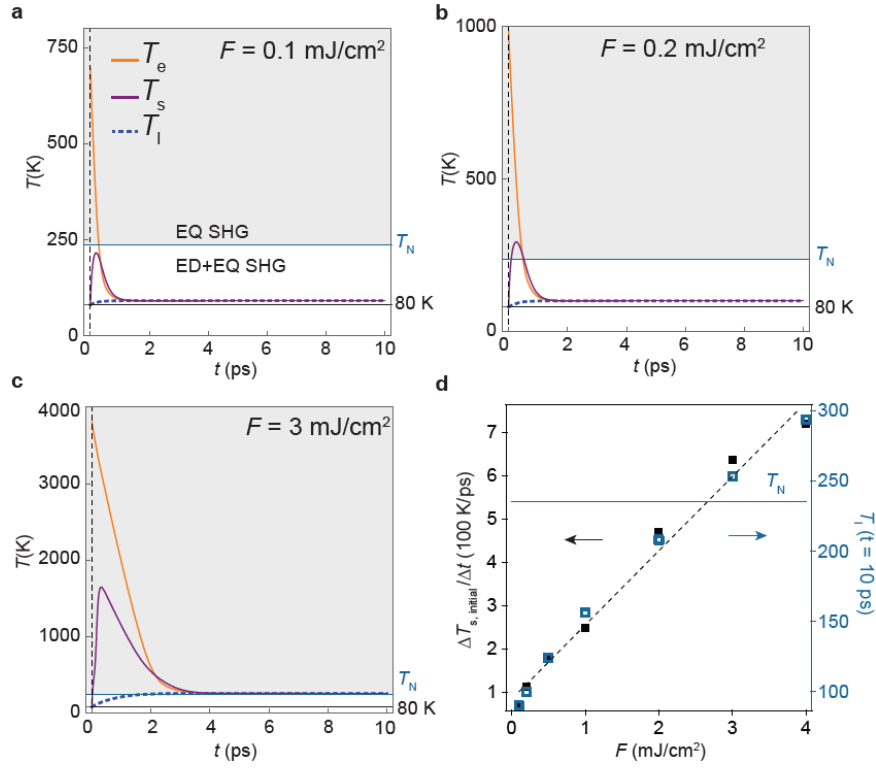


Figure S3. **a-c**, Solutions to the 3TM for an initial temperature $T = 80$ K at representative F values. White (gray) region denotes where one expects ED + EQ (just EQ) SHG contributions. The fluences corresponding to the three regimes in a-c will change depending on the chosen g values, but the trends stay the same. **d**, The rate of change of T_s extracted from a linear fit to the initial decay (< 1 ps) after the maximum (black), and the final equilibrated temperature (blue), plotted as a function of F .

S4. Coherent in-plane magnon in the $F > F_c$ regime

We observe coherent oscillations of the in-plane magnon mode with symmetry B_{2g} in the MOKE transients for $F > F_c$, albeit with a lifetime limited to several picoseconds, despite the absence of long-range inter-plane magnetic correlations. This in-plane magnon mode involves a precession of the $J_{\text{eff}} = 1/2$ moments out of the plane, which produces the observed oscillations in the MOKE transients [10] and does not depend on inter-plane magnetic correlations. This is consistent with previous time-resolved RIXS studies [11] and static RIXS measurements on La-doped Sr_2IrO_4 [12, 13] showing that in-plane magnon modes survive even in the absence of 3D long-range ordering, albeit with shorter lifetime. The source of these transient MOKE oscillations is not to be confused with the source of the static MOKE signal that occurs in finite magnetic field, which is sensitive to the bulk magnetization and thus *does* depend on having inter-plane + + + + magnetic correlations [5].

As discussed in Ref. [3], the zero-field SHG response is sensitive to the in-plane surface magnetization of the $- + + -$ state. Since the in-plane magnon mode involves precession of the $J_{\text{eff}} = 1/2$ moments out of the plane, this will cause the in-plane projection of the magnetization to also oscillate, which should in principle be detectable by time-resolved SHG. However, unlike in MOKE, we do not observe coherent magnon induced oscillations in the transient SHG response likely for the following reasons. Since MOKE probes the out-of-plane moment ($\propto \sin \theta$) whereas SHG probes the in-plane moment ($\propto \cos \theta$), where θ is the small canting angle away from the plane, the MOKE and SHG signals scale like θ and $1 - \theta^2/2$ respectively. Moreover, our MOKE setup uses lock-in detection whereas the SHG does not. These differences make MOKE inherently more sensitive to the coherent B_{2g} magnon oscillations compared to SHG.

S5. Time-resolved SHG transients for $F > F^*$

As the quartic potential transforms into a parabolic potential above F^* , the internal dynamics of the magnetic degrees of freedom should again speed up above F^* . In principle, a probe capable of measuring magnetic excitation lifetimes in the paramagnetic regime ($F > F^*$) should detect such a speed up. However, our SHG-RA probe can only sense excitation lifetimes of the AFM order parameter, which is zero for $F > F^*$. Therefore, we expect the SHG transients to remain slow for all F greater than F^* , which is indeed what we observe (Fig. S4).

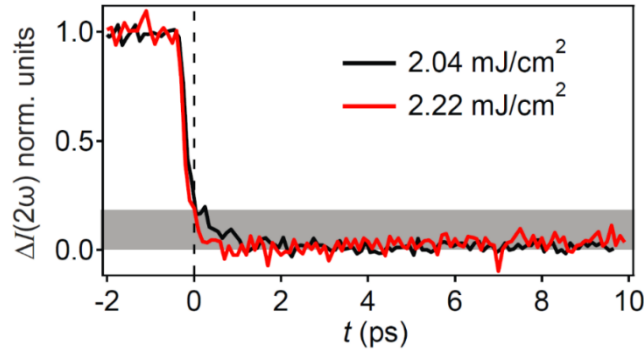


Figure S4. SHG transients acquired at $T = 80$ K for fluences near and above $F^* \sim 1.6 \text{ mJ/cm}^2$ under the same conditions as shown in Fig. 3 a,b in the main text. The height of the grey bar denotes the excess EQ SHG intensity induced by magneto-elastic distortions.

We also elaborate on the possible explanation for the slower exponential drop after $t = 0$ that is apparent at high fluences. In thermal equilibrium, Sr_2IrO_4 undergoes lattice deformations across T_N due to magneto-elastic coupling [14, 4], which become more pronounced as the MOP increases. Therefore, below T_N , not only is there an onset of magnetization-induced ED SHG but also a change in the existing EQ SHG tensor elements induced by lattice deformations [15, 16]. Upon photo-excitation, one expects the lattice deformations to partially or fully relax in response to a partial or full melting of the MOP respectively. However, since the suppression of magnetic ordering by photo-doping occurs on a timescale (< 0.3 ps) that is much faster than the lattice relaxation time ($\sim 1\text{-}2$ ps) [17, 18], the extent to which the lattice is able to relax will depend on the timescale τ for the MOP to recover. For example, if $\tau \ll 1\text{-}2$ ps, then the lattice will not have sufficient time to relax and will thus be frozen in its initial state. Conversely, if $\tau \gg 1\text{-}2$ ps, then the lattice can relax to the full extent allowed by the transient value of the MOP. In our experiments, the regime where $\tau \gg 1\text{-}2$ ps is only achieved when F approaches F^* , which is why those SHG transients show the slow lattice relaxation component most clearly (Fig. S4). For lower fluences, not only does τ become shorter but the MOP also becomes suppressed by smaller amounts. Therefore, although a finite lattice relaxation component must still exist in this regime, it constitutes a much smaller fraction of the overall SHG signal, making it difficult to resolve.

S6. Ruling out alternative explanations for slow dynamics

In this section we discuss other mechanisms that were considered towards explaining the slow recovery of the MOP in Sr_2IrO_4 and why they were ruled out.

1. Near-degeneracy of different c -axis stacking arrangements It has been reported that there are several stacking arrangements of the AFM ordered layers along the c -axis that may be close in energy and challenging to distinguish using diffraction based techniques alone [4, 19, 20, 21]. Therefore, one may ask whether after destroying c -axis magnetic correlations with the pump beam, the system, in the process of recovery, becomes trapped in some metastable stacking arrangement, which returns to the true ground state only through a slow annealing process. There are two arguments that can be used to rule out this scenario: (i) The c -axis correlations are destroyed at F_c , yet the recovery dynamics remain fast with no anomalous change at F_c ; (ii) For the scenario proposed one would expect a discontinuous jump in the recovery time at the point where c -axis correlations are destroyed. However, we observe a power law type increase of τ upon approaching F^* , not a sudden jump.

2. Healing of topological defects Topological defects in an order parameter field created by spatially localized absorption of photons have recently been invoked to explain the slow recovery dynamics in photo-excited charge density wave materials [22]. However, time-resolved x-ray scattering measurements on Sr_2IrO_4 report no transient broadening of the magnetic diffraction peak and thus no reduced correlation length [11]. Moreover, if the suppression of the MOP in Sr_2IrO_4 was related to the presence of topological defects (vortex/anti-vortex pairs) in the spin texture created by the pump, then the defect density would be proportional to the pump fluence. However, the equilibration rate of topological defects (i.e., recombination rate of vortex/anti-vortex pairs), is proportional to their density. Therefore, one would expect that the recovery rate increases linearly with pump fluence. This is opposite to our observed behavior in Sr_2IrO_4 , where the recovery rate decreases with pump fluence, which rules out this scenario.

Another scenario is related to the Kibble-Zurek mechanism [23] where topological defects are created as the system relaxes from the pump-induced paramagnetic state back into the AFM state. Here one would expect the recovery to suddenly become very slow once the system is pumped into the paramagnetic state. However, we do not observe any drastic slowing down of the recovery across F_c , ruling out this mechanism.

3. Slow relaxation of the magneto-elastic deformation We consider here a hypothetical scenario in which there is a critical lattice deformation amplitude above which magnetic long-range order is not supported. In this scenario, the critical amplitude would be reached when $F > F^*$, and the time required for the lattice to relax back below the critical amplitude thus becomes the bottleneck for the recovery of magnetic order. For the following reasons, we rule out this scenario. (1) If this scenario were correct, then one would expect a discontinuous jump in the SHG recovery time at F^* . Instead, we observe a power law increase upon approaching F^* . (2) If this scenario were correct, then one would expect the magnetization-induced ED SHG contribution to suddenly reappear at the instant the lattice relaxes across the critical amplitude, resulting in a discontinuity in the slope of the SHG transient. However, we do not observe any such discontinuity. (3) Recent studies show that magnetic order in Sr_2IrO_4 is robust against substantial lattice deformation imparted by both compressive and tensile epitaxial strain [24], applied uniaxial strain [25] and hydrostatic pressure up to ~ 17 GPa [26].

S7. Details of the Langevin theory

We derive equations of motion for our magnetic degrees of freedom starting from a Hamiltonian by building on the standard approach to studying dynamical critical phenomena at finite temperature developed by Hohenberg and Halperin [27, 28]. To describe the thermalization of the z -axis magnons, we start with the following Hamiltonian:

$$H[\varphi] = \frac{1}{2} \int dz \left\{ [\nabla_z \varphi(z, t)]^2 + \tau_0^{-1} \varphi^2(z, t) + \frac{\lambda}{2} \varphi^4(z, t) \right\}$$

where $\varphi(z, t)$ is a real bosonic scalar field that parameterizes how the intralayer Néel vector varies along the z -axis, τ_0^{-1} is a temperature-dependent mass term that is proportional to the deviation from the mean-field transition temperature, and λ is a purely real coupling constant. The Hamiltonian can be expressed in terms of its Fourier components in the following way:

$$H[\varphi] = \frac{V}{2} \int \frac{dk}{2\pi} (k^2 + \tau_0^{-1}) \varphi_{-k} \varphi_k + \frac{\lambda V}{4} \int \frac{dk_1}{2\pi} \int \frac{dk_2}{2\pi} \int \frac{dk_3}{2\pi} \varphi_{k_1} \varphi_{k_2} \varphi_{k_3} \varphi_{-k_1-k_2-k_3}$$

where φ_k is the k^{th} Fourier component of the order parameter field and V is the volume. The relaxation dynamics of the system can then be studied through the Langevin equation:

$$\partial_t \varphi_k(t) = -\frac{1}{V} \frac{\delta\{H[\varphi_k(t)]\}}{\delta\varphi_{-k}(t)} + \xi_k(t)$$

where $\xi_k(t)$ is a Gaussian noise term with $\langle \xi_k(t) \rangle = 0$ and $\langle \xi_k(t) \xi_{k'}(t') \rangle = \delta(t - t') \delta(k + k') (k^2 + \tau_0^{-1}) [2n_k(t) + 1]$, which describes fluctuations and imprints a non-equilibrium fluctuation-dissipation relation for some general distribution function $n_k(t)$. In the case of thermal equilibrium $n_k(t)$ is simply the Bose-Einstein distribution that, in the high temperature (T) limit, can be expanded as $2n_k(t) + 1 \approx 2T/(k^2 + \tau_0^{-1})$, which is precisely the regime considered in the seminal work by Hohenberg and Halperin [27] (model A) where fluctuations are simply proportional to T . In our study, we keep the noise in this more general form that one would derive based on the Keldysh formalism. Explicitly writing out the Langevin equation leads to the form shown in the manuscript:

$$\partial_t \varphi_k(t) = -(k^2 + \tau_0^{-1}) \varphi_k(t) - \lambda \int \frac{dk_1}{2\pi} \int \frac{dk_2}{2\pi} \varphi_{k_1}(t) \varphi_{k_2}(t) \varphi_{k-k_1-k_2}(t) + \xi_k(t)$$

Starting from this equation, the first-order perturbative (Hartree shift) correction to the mass (i.e. the relaxation time) is given by $\tau^{-1} = \tau_0^{-1} - \lambda \int d\omega \rho(\omega) n(\omega) = \tau_0^{-1} - \lambda N_{mag}$, where $\rho(\omega)$ is the magnon density of states, $n(\omega)$ is their distribution function versus energy ω , and N_{mag} is the total number of magnons. In thermal equilibrium, increasing temperature increases the magnon number and thus also the decay time, with the thermal critical point located at $\tau^{-1} = 0$.

We are specifically interested in studying a general magnon distribution function $n_k(t)$ that is non-thermal and changes in time following the linearized Boltzmann equation:

$$\partial_t n_k(t) = -|\tau^{-1}| [n_k(t) - n_k^T]$$

where n_k^T is the equilibrium Bose-Einstein distribution function at temperature T and τ is the thermalization time. We note that the distribution function of course describes a fully 3D system and so ordering is allowed at finite temperatures. But since the rate-limiting step is thermalization along the z -axis, we are defining $n_k(t)$ as the distribution function after integrating out the x and y components. This equation governs how quickly an out-of-equilibrium magnon distribution function thermalizes back to Bose-Einstein form for some fixed energy content corresponding to temperature T . Up to leading order, the lifetime of a magnetic excitation (given by the mass of the potential expressed in the Hamiltonian above) is also the average lifetime of a deviation from the Bose-Einstein distribution function. This can be rigorously proven through a systematic derivation of the Boltzmann equation using the Keldysh formalism, which shows that the relaxation time in a linearized Boltzmann equation in general is given by the imaginary part of the retarded self-energy [for details see for example Ref. [29] sec. V.B.; Ref [30] sec. 3.5; Ref [31] sec. III]. This means that the timescale τ found in the Boltzmann equation is equivalent to the τ derived from our Hamiltonian. For $\tau > 0$ the magnons want to enter the ordered phase with an order parameter $\langle \varphi \rangle \sim 1/\sqrt{\tau\lambda}$. Note that one would typically expect the order parameter to be defined by $1/\sqrt{\tau\lambda}$ in equilibrium (i.e. when τ is time independent).

An interesting consequence of these equations is that the relaxation time (and therefore the distance to the critical point) is susceptible to the number of magnons in the system but not to the total energy in the system. In thermal equilibrium, there is, of course, a one-to-one correspondence between the total magnon number (N_{mag}) and total magnon energy (E_{mag}), related through the temperature of the system T . For a generic density of states of the form:

$$\rho(\omega) = \rho_0 \omega^\alpha$$

for some power $\alpha > 1$ (again the system is physically three-dimensional), the magnon number and energy are given by:

$$\begin{aligned} N_{mag} &= \rho_0 T^{1+\alpha} f(\alpha) \\ E_{mag} &= \rho_0 T^{2+\alpha} f(\alpha + 1) \end{aligned}$$

where $f(\alpha) = \alpha\Gamma(\alpha)\zeta(\alpha + 1)$, with $\zeta(\alpha)$ the Riemann zeta-function and $\Gamma(\alpha)$ the gamma-function. In thermal equilibrium, N_{mag} and E_{mag} are related such that they yield the same value for T . In stark contrast, when driven away from equilibrium, N_{mag} and E_{mag} are not constrained to be related via the Bose-Einstein distribution anymore and the two equations may define two different effective temperatures, which we call T_{num} and T_{en} respectively. To illustrate the consequences of this behaviour in an intuitive way and show how it explains our experimental observations, we consider the three different regimes of our experiment and a simplified out-of-equilibrium distribution for the magnon degrees of freedom:

(1) **Initial $t < 0$ regime** before the system is pumped: the magnons are in thermal equilibrium at an initial temperature T_i below the 3D AFM ordering temperature T_N and are described by a Bose-Einstein distribution $n^{B.E.}(\omega/T_i)$.

(2) **Quenched regime** immediately after the pump pulse is switched off: the pump creates a large density of magnons through the charge relaxation process, which modifies its distribution function. For ease of calculation, we assume that immediately after the pumping stage, the magnon distribution is $n(\omega) = n^{B.E.}(\omega/T_i) + N_{pump} \delta(\omega - \omega_0)$, i.e. it has an extra number of magnons N_{pump} at some energy ω_0 introduced by the pump beam. But our results are valid for general more complicated non-equilibrium distribution functions. This leads to the following expressions:

$$N_{mag} = \rho_0 T_i^{1+\alpha} f(\alpha) + N_{pump} \rho_0 \omega_0^\alpha \equiv \rho_0 T_{num}^{1+\alpha} f(\alpha)$$

$$E_{mag} = \rho_0 T_i^{2+\alpha} f(\alpha + 1) + N_{pump} \rho_0 \omega_0^{\alpha+1} \equiv \rho_0 T_{en}^{2+\alpha} f(\alpha + 1)$$

where we defined the corresponding effective temperatures associated with the magnon number and energy. In principle $T_{num} \neq T_{en}$. Since $T_{num} > T_i$, the order parameter is suppressed.

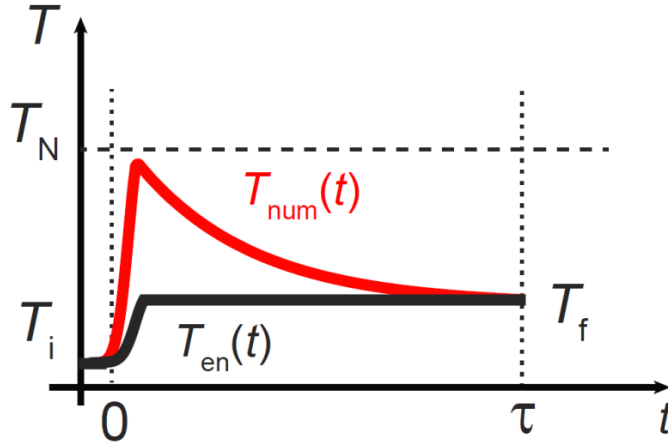


Figure S5. Schematic of the temporal evolution of the effective temperatures T_{num} and T_{en} after pump excitation corresponding to the experimental regime $F < F^*$. The peak in the temperature curves occur after magnons are emitted following charge relaxation, hence they are delayed from $t = 0$.

(3) **Relaxation regime:** Magnon collisions lead to equilibration between the different magnon modes, which allows the magnon distribution function to relax back towards a Bose-Einstein distribution $n^{B.E.}(\omega/T_f)$, albeit at a higher final temperature T_f . Since the energy is conserved this must be $T_f = T_{en}$. After relaxation, N_{mag} and E_{mag} are again determined by the same temperature T_f . The three stages can be expressed via the effective temperature in the magnon particle number $T_i \rightarrow T_{num} \rightarrow T_{en}$ (Fig. S5). The key insight in the proposed mechanism is that T_{num} can be brought rather close to the critical temperature T_N through pumping while both T_i and T_{en} remain below T_N . Thus, the system becomes trapped in a non-equilibrium critical state that suppresses the relaxation of the out-of-equilibrium magnon distribution, although the energy density is far from criticality. This is precisely the situation realized in our experiments near F^* . Both equilibria (before and long after the pump) are non-critical (see section S3), yet the intermediate non-equilibrium state mimics criticality for a transient time regime. The equilibration times can be explicitly solved in this simplified model to yield:

$$\begin{aligned}
\tau^{-1}(t < 0) &= \tau_0^{-1} - \lambda \int d\omega \rho(\omega) n^{B.E.}(\omega/T_i) \\
\tau^{-1}(t > 0) &= \tau^{-1}(t < 0) - \lambda N_{pump} \rho(\omega_0) \\
\tau^{-1}(t \gg 0) &= \tau_0^{-1} - \lambda \int d\omega \rho(\omega) n^{B.E.}(\omega/T_f)
\end{aligned}$$

The effect observed in our experiments can be seen through the expression for $\tau^{-1}(t > 0)$, which shows that at some critical pump intensity (corresponding to F^* in our experiments), the relaxation rate goes to zero. The physical picture behind this mechanism is the following: Photo-doping occurs immediately upon pump excitation and causes a reduction of the magnetic order parameter in proportion to the number of photo-carriers. In contrast, the magnon number is proportional to the energy released when the photo-carriers subsequently decay. This means that the critical fluences for collapsing the magnetic order via photo-doping and magnon generation, F_c and F^* respectively, are generally different. The relaxation of the photo-carriers populates magnon modes around $\omega \approx \omega_0$. Now the system wants to relax towards its equilibrium state. This happens via local scattering processes that both generate magnon modes (“in-scattering”) and destroy magnon modes (“out-scattering”). For a system away from a critical point, out-scattering into the continuum is typically much larger and the system acquires an effective mass. Here, however, the huge population of magnon modes around $\omega \approx \omega_0$ leads to a compensation of in- and out-scattering, i.e., to a temporarily vanishing mass. Only when the magnon peak has considerably decayed is the mass effectively restored. Since the relaxation rate of the 3D AFM order parameter is given exactly by the mass, it is restored on the same slow timescale.

To verify that a regime where $T_{num} > T_{en}$ as shown in Fig. S5 indeed exists, we write out the formal expression for N_{mag} and E_{mag} in our model above to find:

$$\begin{aligned}
T_{num} &= T_i \left(1 + \frac{N_{pump} \omega_0^\alpha}{T_i^{\alpha+1} f(\alpha)} \right)^{\frac{1}{\alpha+1}} \\
T_{en} &= T_i \left(1 + \frac{N_{pump} \omega_0^{\alpha+1}}{T_i^{\alpha+2} f(\alpha+1)} \right)^{\frac{1}{\alpha+2}}
\end{aligned}$$

Defining $X = \frac{N_{pump} \omega_0^\alpha}{T_i^{\alpha+1} f(\alpha)}$ and $y = \frac{\omega_0}{T_i}$, the condition for $T_{num} > T_{en}$ becomes

$$\left(1 + Xy \frac{f(\alpha)}{f(\alpha+2)} \right)^{\frac{\alpha+1}{\alpha+2}} < 1 + X$$

Since $\frac{\alpha+1}{\alpha+2} < 1$, there is always an X_c such that for $X > X_c$, the above condition is satisfied.

S8. Restoration of the initial SHG-RA pattern after relaxation

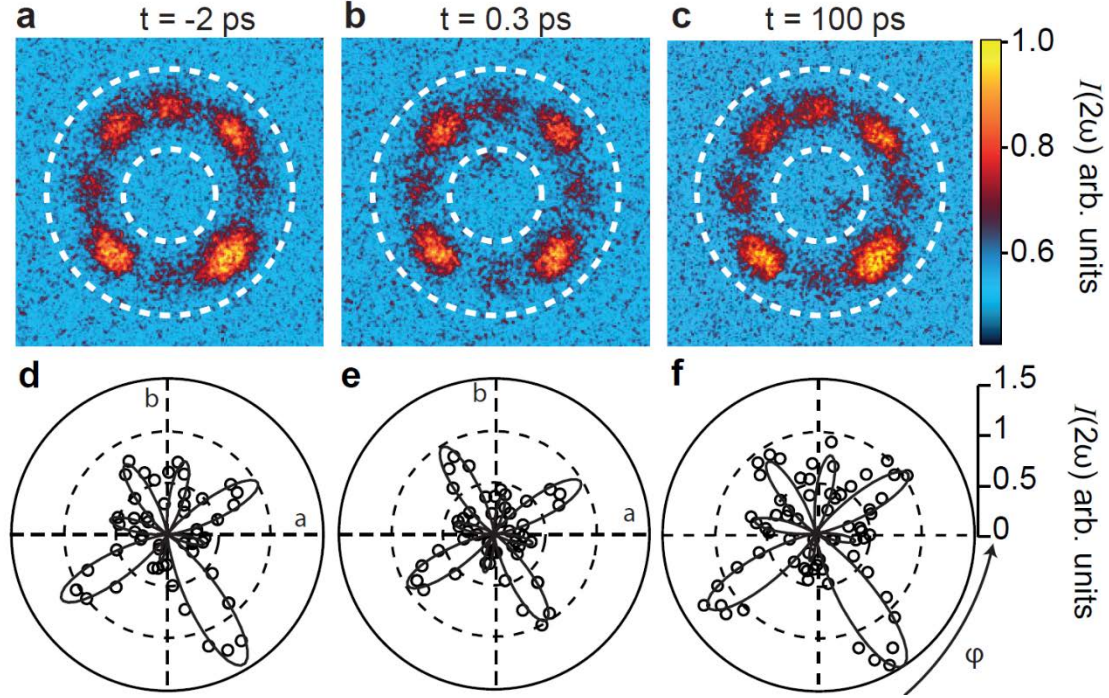


Figure S6. Raw SHG-RA data acquired from a single magnetic domain ($T = 80$ K) in $P_{in}\text{-}S_{out}$ geometry with $n_{ex} = 0.095$ at **a**, $t = -2$ ps, **b**, $t = 0.3$ ps and **c**, $t = 100$ ps. Radially integrated data are shown below in **d**, **e**, and **f**. Recovery of the initial magnetic order (compare **d** and **f**) is observed. Solid lines are fits to the ED and EQ SHG expressions described in the main text.

In zero magnetic field, there are four energetically equivalent magnetic domains in Sr_2IrO_4 , corresponding to four possible orientations of the surface ferromagnetic moment and thus four possible orientations of the large SHG lobe [32, 3]. To ensure that the original magnetic order and domain orientation is recovered even after pumping to above F^* , we focus our pump and probe beams inside a single domain, identified via SHG imaging. To verify this, we show instantaneous SHG-RA data acquired for $F > F^*$ before, immediately after and long after pump excitation in Fig. S6. To convert the raw CCD images into polar SHG-RA plots, data were radially integrated between the white dashed lines. Clearly the original domain orientation is recovered by $t = 100$ ps.

We note that the same magnetization-induced surface ED response can in principle arise from alternative stacking orders such as $++++$ and $-+-+$. However, the former generates an additional strong bulk magnetic-dipole SHG term because it possesses a net bulk magnetization [3], and the latter allows an additional bulk electric-dipole SHG term because it breaks inversion symmetry. Since we do not observe a transient appearance of additional SHG contributions upon pumping, we can also rule out a change from $-++-$ to one of these alternative stacking orders.

S9. Time-resolved SHG transients for different polarization channels

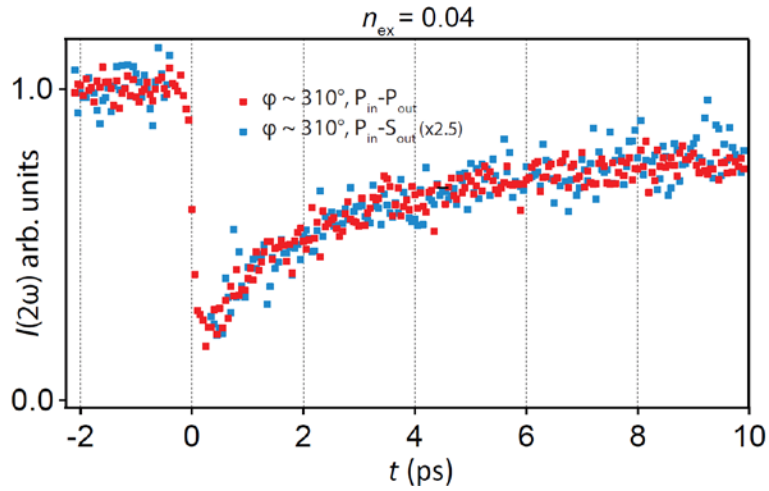


Figure S7. SHG intensity versus time acquired at a fixed value of pump fluence and scattering plane angle φ for two different polarization geometries, which show identical relaxation dynamics.

The SHG dynamics observed in Fig. 3 of the main text were consistently observed under different polarization geometries and different scattering plane angles. Figure S7 shows a direct comparison of the SHG transient acquired under $P_{in}-S_{out}$ and $P_{in}-P_{out}$ geometries. This is expected since all elements of the ED SHG tensor are proportional to the MOP.

Bibliography

- [1] Lee, J. S., Krockenberger, Y., Takahashi, K. S., Kawasaki, M. & Tokura, Y. Insulator-metal transition driven by change of doping and spin-orbit interaction in Sr_2IrO_4 . *Phys. Rev. B* **85**, 035101 (2012).
- [2] Nichols, J. *et al.* Anisotropic electronic properties of *a*-axis-oriented Sr_2IrO_4 epitaxial thin-films. *Appl. Phys. Lett.* **103**, 131910 (2013)
- [3] Seyler, K.L. *et al.*, “Spin-orbit-enhanced magnetic surface second-harmonic generation in Sr_2IrO_4 ,” *Phys. Rev. B* **102**, 201113 (R) (2020).
- [4] Porras, J. *et al.* Pseudospin-lattice coupling in the spin-orbit Mott insulator Sr_2IrO_4 . *Phys. Rev. B* **99**, 085125 (2019).
- [5] Afanasiev, D. *et al.* Ultrafast Spin Dynamics in Photodoped Spin-Orbit Mott Insulator Sr_2IrO_4 . *Phys. Rev. X* **9**, 021020, (2019).
- [6] Beaurepaire, E., Merle, J.-C., Daunois, A. & Bigot, J.-Y. Ultrafast Spin Dynamics in Ferromagnetic Nickel. *Phys. Rev. Lett.* **76**, 4250 (1996).
- [7] Kini, N. S., Strydom, A. M., Jeevan, H. S., Geibel, C. & Ramakrishnan, S. Transport and thermal properties of weakly ferromagnetic Sr_2IrO_4 . *J. Phys. Condens. Matter* **18**, 8205–8216 (2006).
- [8] Hofmann, M. *et al.* Evidence for a large magnetic heat current in insulating layered cuprates. *Phys. Rev. B* **67**, 184502 (2003).
- [9] Shen, X., Timalisina, Y. P., Lu, T.-M. & Yamaguchi, M. Experimental study of electron-phonon coupling and electron internal thermalization in epitaxially grown ultrathin copper films. *Phys. Rev. B* **91**, 045129 (2015).
- [10] Seifert, U. F. P. & Balents, L. Optical excitation of magnons in an easy-plane antiferromagnet: Application to Sr_2IrO_4 . *Phys. Rev. B* **100**, 125161 (2019).
- [11] Dean, M. P. M. *et al.* Ultrafast energy- and momentum-resolved dynamics of magnetic correlations in the photo-doped Mott insulator Sr_2IrO_4 . *Nat. Mater.* **15**, 601–605 (2016); Krupin, O. *et al.*, Ultrafast dynamics of localized magnetic moments in the unconventional Mott insulator Sr_2IrO_4 . *J. Phys.: Condens. Matter* **28**, 32LT01 (2016).
- [12] Gretarsson, H. *et al.* Persistent Paramagnons Deep in the Metallic Phase of $\text{Sr}_{2-x}\text{La}_x\text{IrO}_4$. *Phys. Rev. Lett.* **117**, 107001 (2016).

- [13] Pincini, D. *et al.* Anisotropic exchange and spin-wave damping in pure and electron-doped Sr_2IrO_4 . *Phys. Rev. B* **96**, 075162 (2017).
- [14] Bhatti, I. N., Rawat, R., Banerjee, A. & Pramanik, A. K. Temperature evolution of magnetic and transport behavior in 5d Mott insulator Sr_2IrO_4 : Significance of magneto-structural coupling. *J. Phys. Condens. Matter* **27**, (2014).
- [15] Ron, A., Zoghlin, E., Balents, L., Wilson, S. D. & Hsieh, D. Dimensional crossover in a layered ferromagnet detected by spin correlation driven distortions. *Nat. Commun.* **10**, 1654, (2019).
- [16] Bauer, K.-D. & Hingerl, K. Bulk quadrupole contribution to second harmonic generation from classical oscillator model in silicon. *Opt. Express* **25**, 26567 (2017).
- [17] Li, R. *et al.* Ultrafast time-resolved structural changes of thin-film ferromagnetic metal heated with femtosecond optical pulses. *J. Chem. Phys.* **151**, (2019).
- [18] Li, R. *et al.* Transient lattice deformations of crystals studied by means of ultrafast time-resolved x-ray and electron diffraction. *Struct. Dyn.* **5**, (2018).
- [19] Clancy, J. P. *et al.* Dilute magnetism and spin-orbital percolation effects in $\text{Sr}_2\text{Ir}_{1-x}\text{Rh}_x\text{O}_4$. *Phys. Rev. B* **89**, 054409 (2014)
- [20] Di Matteo, S. & Norman, M. R. Magnetic ground state of Sr_2IrO_4 and implications for second-harmonic generation. *Phys. Rev. B* **94**, 075148 (2016)
- [21] Kim, B. J. *et al.* Phase-Sensitive Observation of a Spin-Orbital Mott State in Sr_2IrO_4 . *Science*. **323**, 1329–1332 (2009)
- [22] Zong, A. *et al.* Evidence for topological defects in a photoinduced phase transition. *Nat. Phys.* **15**, 27 (2019).
- [23] Zurek, W. H. Cosmological experiments in condensed matter systems. *Phys. Rep.* **276**, 177–221 (1996).
- [24] Kim, J. W. *et al.* Controlling symmetry of spin-orbit entangled pseudospin state through uniaxial strain. *Phys. Rev. B* **102**, 054420 (2020).
- [25] Paris, E. *et al.* Strain engineering of the charge and spin-orbital interactions in Sr_2IrO_4 . *PNAS* **117**, 24764 (2020).
- [26] Haskel, D. *et al.* Possible Quantum Paramagnetism in Compressed Sr_2IrO_4 . *Phys. Rev. Lett.* **124**, 67201 (2020).

- [27] Hohenberg, P. C. & Halperin, B. I. Theory of dynamic critical phenomena. *Rev. Mod. Phys.* **49**, 435–479 (1977).
- [28] Dolgirev, P. E., Michael, M. H., Zong, A., Gedik, N. & Demler, E. Self-similar dynamics of order parameter fluctuations in pump-probe experiments. *Phys. Rev. B* **101**, 174306 (2020).
- [29] Sieberer, L. M., Buchhold, M. & Diehl, S. Keldysh field theory for driven open quantum systems. *Reports Prog. Phys.* **79**, 096001 (2016).
- [30] Kamenev, A. & Levchenko, A. Keldysh technique and non-linear σ -model: basic principles and applications. *Adv. Phys.* **58**, 197–319 (2009).
- [31] Kamenev, A. Many-body theory of non-equilibrium systems. *arXiv:cond-mat/0412296* (2004).
- [32] Zhao, L. *et al.* Evidence of an odd-parity hidden order in a spin-orbit coupled correlated iridate. *Nat. Phys.* **12**, 32–36 (2016).